Ultra-strong and ductile precipitation-strengthened high entropy alloy with 0.5% Nb addition produced by laser additive manufacturing

Wei Zhang , Ali Chabok , Hui Wang , Jiajia Shen , J.P. Oliveira ,
Shaochuan Feng , Nobert Schell , Bart J. Kooi , Yutao Pei

PII: S1005-0302(24)00055-0
DOI: https://doi.org/10.1016/j.jmst.2023.11.053
Reference: JMST 5352

To appear in: *Journal of Materials Science & Technology*

Received date: 10 August 2023
Revised date: 19 November 2023
Accepted date: 20 November 2023

Please cite this article as: Wei Zhang , Ali Chabok , Hui Wang , Jiajia Shen , J.P. Oliveira , Shaochuan Feng , Nobert Schell , Bart J. Kooi , Yutao Pei , Ultra-strong and ductile precipitation-strengthened high entropy alloy with 0.5% Nb addition produced by laser additive manufacturing, *Journal of Materials Science & Technology* (2024), doi: https://doi.org/10.1016/j.jmst.2023.11.053

Highlights

- Nb-added interstitial solute-strengthened high entropy alloy (iHEA) was synthesized in situ by laser melting deposition
- Incorporation of Nb promotes solid solution strengthening, grain boundary strengthening, and precipitation strengthening
- An exceptional combination of strength (1450 MPa) and elongation (30%) was achieved
- Enhanced micromechanical properties of grains with different orientations were obtained despite the reduced twinning activity

Research Article

Ultra-strong and ductile precipitation-strengthened high entropy alloy with 0.5% Nb addition produced by laser additive manufacturing

Wei Zhang [a, 1], Ali Chabok [a, 1], Hui Wang [b], Jiajia Shen [c, d], J.P. Oliveira [c, d], Shaochuan Feng [e], Nobert Schell [f], Bart J. Kooi [b], Yutao Pei [a, *]

[a] Advanced Production Engineering, Engineering and Technology Institute Groningen, Faculty of Science and Engineering, University of Groningen, Nijenborgh 4, 9747 AG, Netherlands

[b] Nanostructured Materials and Interfaces, Zernike Institute for Advanced Materials, Faculty of Science and Engineering, University of Groningen, Nijenborgh 4, 9747 AG, Netherlands

[c] UNIDEMI, Department of Mechanical and Industrial Engineering, NOVA School Science and Technology, Universidade NOVA de Lisboa, Caparica 2829-516, Portugal

[d] CENIMAT/I3N, Department of Materials Science, NOVA School of Science and Technology, Universidade NOVA de Lisboa, 2829-516 Caparica, Portugal

[e] School of Mechanical Engineering, University of Science and Technology Beijing, Beijing 100083, China

[f] Institute of Materials Physics, Helmholtz-Zentrum Hereon, Max-Planck-Str. 1, Geesthacht, D-21502, Germany

[1] These authors contributed equally to this work.

* Corresponding author.

E-mail address: y.pei@rug.nl (Y.T. Pei).

Abstract

Achieving a superior strength-ductility combination for fcc single-phase high entropy alloys (HEAs) is challenging. The present work investigates the in-situ synthesis of $Fe_{49.5}Mn_{30}Co_{10}Cr_{10}C_{0.5}$ interstitial solute-strengthened HEA containing 0.5 wt.% Nb (hereafter referred to as iHEA-Nb) using laser melting deposition (LMD), aiming at simultaneously activating multiple strengthening mechanisms. The effect of Nb addition on the microstructure evolution, mechanical properties, strengthening, and deformation mechanisms of the as-deposited iHEA-Nb samples was comprehensively evaluated. Multiple levels of heterogeneity were observed in the LMD-deposited microstructure, including different grain sizes, cellular subgrain structures, various carbide precipitates, as well as elemental segregation. The incorporation of Nb atoms with a large radius leads to lattice distortion, reduces the average grain size, and increases the types and fractions of carbides, aiding in promoting solid solution strengthening, grain boundary strengthening, and precipitation strengthening. Tensile test results show that the Nb addition significantly increases the yield strength and ultimate tensile strength of the iHEA to 1140 and 1450 MPa, respectively, while maintaining the elongation over 30%. Deformation twins were generated in the tensile deformed samples, contributing to the occurrence of twinning-induced plasticity. This outstanding combination of strength and ductility exceeds that for most additively manufactured HEAs reported to date, demonstrating that the present *in situ* alloying strategy could provide significant advantages for developing and tailoring microstructures and balancing the mechanical properties of HEAs while avoiding conventional complex thermomechanical treatments. In addition, single-crystal micropillar compression tests revealed that although the twining activity is reduced by the Nb addition to the iHEA, the micromechanical properties of grains with different orientations were significantly enhanced.

Keywords: Laser additive manufacturing; high entropy alloy; *in situ* alloying; precipitation strengthening; deformation mechanism; mechanical properties.

1. Introduction

The definition of high entropy alloys (HEAs) is based on multiple component elements with equal or near-equal compositions, differing from traditional alloy systems where various alloying elements are usually added to the principal elements [1, 2]. In recent years, HEAs have been continuously developed. In addition to the common single-phase HEAs, a variety of HEAs including dual-phase, metastable, interstitial- and precipitation-strengthened HEAs have been reported to further improve their mechanical performance [3–7]. Among them, changing the system compositions and adding alloying elements are important methods employed by researchers to overcome the trade-off that typically exists between high strength and high ductility. These alloying elements either lead to grain refinement, new phase formation, or solid solution strengthening. Generally, elements with small atomic radii such as carbon will cause interstitial strengthening, whereas elements with large atomic radii such as Al, Mo, Nb, or Ti, will induce significant solid solution strengthening and precipitation strengthening [8–11]. $Fe_{49.5}Mn_{30}Co_{10}Cr_{10}C_{0.5}$ is an interstitial-strengthened HEA (iHEA) that exhibits excellent mechanical properties due to the simultaneous activation of multiple deformation mechanisms, such as phase transformation/twinning-induced plasticity (TRIP/TWIP) [12, 13].

Among the different HEAs fabrication methods, laser additive manufacturing (LAM), as near-net-shape manufacturing technology with high design flexibility, high production efficiency, and low material waste, is considered a promising method in the HEAs field [14–17]. Among different LAM technologies, laser melting deposition (LMD) based on a powder feeding system, is characterized by high deposition efficiency and rapid solidification rate [18]. Compared with the widely used laser powder bed fusion (LPBF) process, which has strict requirements on the composition of the pre-alloyed HEAs powders, the in-situ synthesis of HEAs during the LMD process allows the addition of other powders and the rapid adjustment of the mixing ratios of different powders, so that the composition and microstructure of the as-built parts can be customized freely and simply. The diversity and variability of HEA components bring more opportunities for the applications of LMD technology.

In the studies of [19–21], γ' and γ'' precipitated phases were successfully introduced in precipitation-hardened HEAs by alloying Al/Ti and Nb, respectively, during the LMD process. Among them, the γ'' phase induced a significant strengthening effect even at a small volume fraction [20], indicating the great potential of Nb alloying in improving the performance of HEAs. Based on previous research findings, the addition of Nb as a trace alloying element in HEAs mainly provides the following benefits: Firstly, it induces severe lattice distortion to promote solid solution strengthening [22, 23]. Secondly, it tends to promote the formation of a hard Laves phase, thereby increasing the precipitation hardening effect [24, 25]. Thirdly, it can also facilitate the formation of a fine eutectic structure and improve performance [24, 26]. These benefits are mainly due to the very negative mixing enthalpy of Nb with other incorporated elements. To the best of the authors' knowledge, the incorporation of Nb in the $Fe_{49.5}Mn_{30}Co_{10}Cr_{10}C_{0.5}$ iHEA alloy matrix has not been reported in the literature. Therefore, it is promising to fabricate both interstitial-strengthened and precipitate-hardened HEA based on the $Fe_{49.5}Mn_{30}Co_{10}Cr_{10}C_{0.5}$ system to achieve excellent mechanical properties.

In the present work, LMD was used for *in situ* synthesis of Nb-containing $Fe_{49.5}Mn_{30}Co_{10}Cr_{10}C_{0.5}$ iHEA, and the effect of Nb alloying on the microstructure evolution, mechanical properties, strengthening, and deformation mechanisms was analyzed. The results revealed that the addition of a small quantity of Nb greatly increases the tensile strength of iHEA while maintaining good plasticity. The detailed strengthening and deformation mechanisms were assessed based on the obtained microstructure, and the deformation behavior of individual crystals, depending on their grain orientation, was also investigated. These findings are expected to contribute to the successful application of Nb-containing HEA in the additive manufacturing field.

2. Experimental

2.1. Sample preparation

The particle morphology of the pre-alloyed $Fe_{49.5}Mn_{30}Co_{10}Cr_{10}C_{0.5}$ iHEA powders is shown in Fig. S1(a) in Supporting Information, with the particle size ranging from 50 to 140 μm. To investigate the effect of Nb addition on the microstructure and mechanical properties of the current iHEA, 0.5 wt.% Nb powder (99.95% purity) was mixed with 99.5 wt.% iHEA powder. The particle morphology of elemental Nb powder is shown in Fig. S1(b). These two powders were mixed in the mixer of the powder feeder for 24 h. The LMD process was carried out using a 3 kW IPF Photonics fiber laser with a wavelength of 1.07 μm. The following optimized printing parameters were used for the fabrication of the iHEA-Nb bulk sample: laser power of 1500 W, scanning speed of 350 mm s^{-1}, and overlap ratio of 50%. A scanning pattern with 180° angle rotation between two consecutive deposition layers was applied, and ST37 carbon steel plates were used as the substrates. The same optimization was also applied to the $Fe_{49.5}Mn_{30}Co_{10}Cr_{10}C_{0.5}$ iHEA reference samples without Nb addition.

2.2. Mechanical testing

For both iHEA-Nb and iHEA reference samples, tensile specimens with gauge dimensions of 11.5 mm × 3.5 mm × 1mm were obtained with the long axes parallel to the laser scanning direction using electrical discharge machining. Prior to the tensile tests, the specimens were sequentially ground using SiC sandpaper from 320 to 2000 grit. Uniaxial tensile tests were conducted using a Kammrath-Weiss tensile module in displacement-controlled mode at the strain rate of 10^{-4} s^{-1}, and the machine displacement was used to measure tensile strain. Tensile tests were repeated at least 3 times for each condition to ensure the reliability and repeatability of the results. *In situ* micropillar compression tests were performed on differently oriented grains ([011] and [111], respectively) to study the micromechanical properties of the as-built iHEA-Nb sample. The micropillars were prepared using a focused ion beam (FIB) and the detailed preparation parameters can be found in our previous work [27].

2.3. Microstructural characterization

The microstructure and elemental distribution of the LMD-built iHEA-Nb samples were characterized by scanning electron microscopy (SEM, Tescan, Czech Republic) coupled with energy dispersive X-ray spectroscopy (EDS). Electron backscatter diffraction (EBSD) was used to analyze the crystallographic orientation, grain size, and kernel average misorientation (KAM) distribution. Phase constituents were identified by high-energy synchrotron X-ray diffraction (SXRD, P07 High Energy Materials Science beamline, Petra III/DESY) for the as-deposited and tensile fractured samples. To analyze the in-situ formed precipitates, transmission electron microscopy (TEM, JEOL-2200FS, JEOL, Japan) was employed with an acceleration voltage of 200 kV. The TEM samples were prepared using FIB in a dual-beam microscope (Helios G4 CX, FEI Co.).

3. Results and discussion

3.1. Microstructure

The EBSD inverse pole figures (IPFs), grain boundaries (GBs), and overall KAM maps from three different cross-views of the LMD-built iHEA-Nb sample are shown in Fig. 1. The current sample shows the frequently observed LMD-built microstructural features of elongated and zig-zag morphology (on the *YOZ* and *XOY* plane, respectively, where the scanning directions are schematically indicated at the bottom left of Fig. 1), which resulted from the change in the maximum heat flow direction as each layer was deposited through rotating the laser scanning direction 180° [28, 29]. The IPF microstructure in the longitudinal sections (*XOZ* and *YOZ* planes) exhibits a typical heterogeneous grain structure consisting of large elongated columnar grains and equiaxed fine grains, where the continuous nucleation of the equiaxed fine grains is detected around the laser trajectory and layer interfaces. Compared to other metal additive manufacturing methods, the LMD process has a relatively low ratio of thermal gradient and growth rate [29–31], leading to the aforementioned grain morphology. The GBs maps are shown in Fig. 1(b), where red, green, and blue represent subgrain boundaries (SubGBs), low-angle grain boundaries (LAGBs), and high-angle grain boundaries (HAGBs), respectively. Most of the grain interiors, especially near SubGBs and LAGBs, exhibit high lattice distortion, implying the accumulation of dislocations in these regions [32]. This can be confirmed by the overall KAM results in Fig. 1(c), revealing high strain levels near grain boundaries. The large atomic radius of the Nb element would cause severe lattice distortion of the iHEA during the rapid cooling and solidification process associated with laser deposition, giving rise to high pulse stress inside the as-built sample. As a result, a high dislocation density was easily generated near the laser trajectories [33, 34]. The iHEA sample without Nb addition also exhibits epitaxial growth and heterogeneous grain structure along the building direction (Fig. S2). However, the iHEA-Nb sample has a higher number of fine grains. During the solidification process, the presence of the Nb element will increase the constitutional undercooling of the liquid and reduce the thermal gradient due to its severe partition between solid and liquid phases [18, 24]. With the fast solidification accompanying the LMD process, crystal nuclei are easily formed in the undercooled melt in front of the columnar dendrites [35], leading to the formation of more fine grains near the laser tracks and layer interfaces.

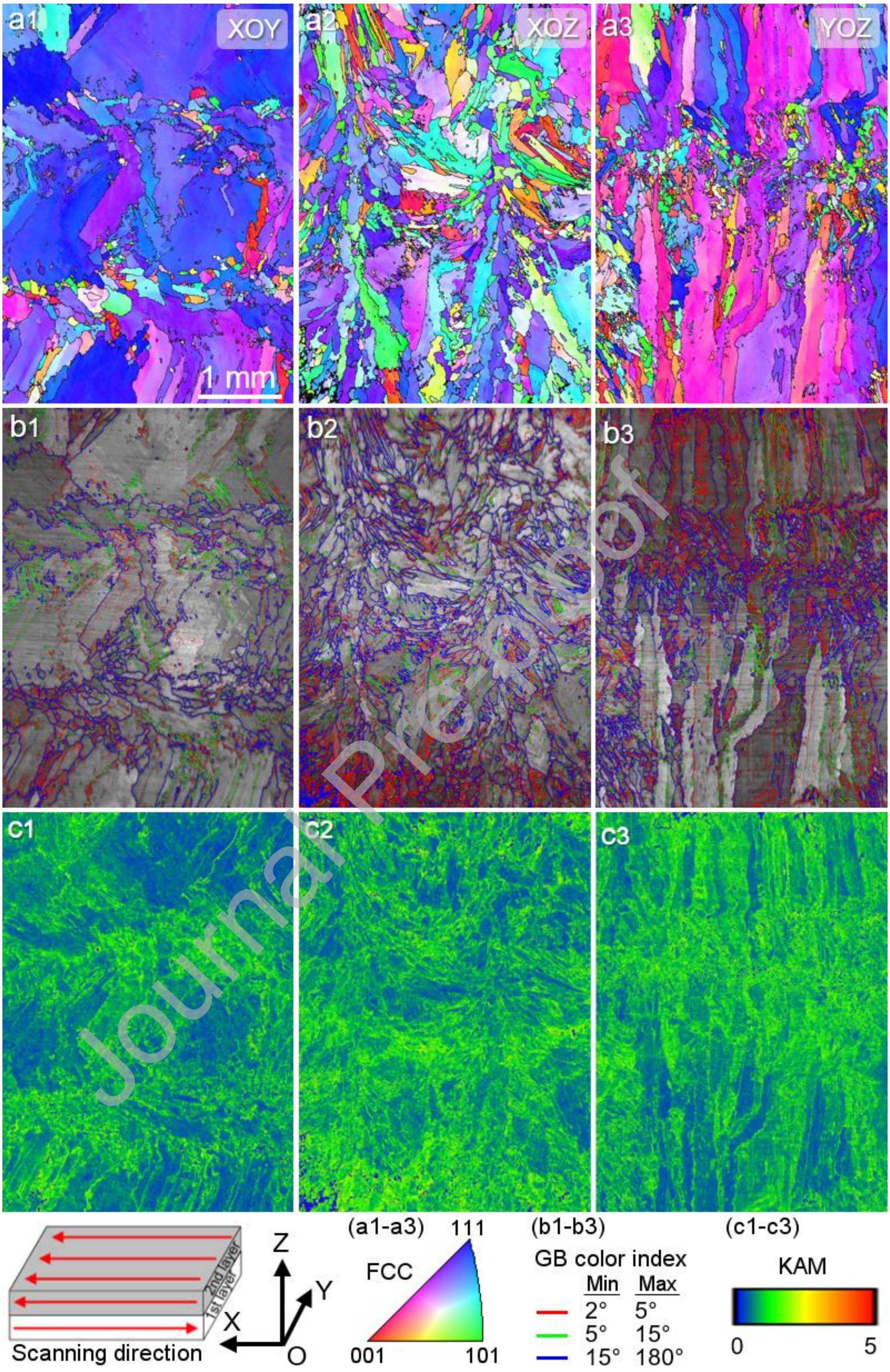

Fig. 1. EBSD results of the LMD-deposited iHEA-Nb sample. (a1–a3) IPF maps plotted relative to the tensile direction, (b1–b3) grain boundary maps, and (c1–c3) KAM maps.

Pole figures (PFs) in the *XOY* plane were identified by EBSD to analyze the texture of the LMD-built iHEA-Nb sample, as presented in Fig. 2. The iHEA-Nb sample shows the highest multiples of uniform density (MUD) in the <111> texture // tensile loading direction (*X*), with a maximum intensity value of 12.74, higher than that of the iHEA reference sample (Fig. S3). In addition, both iHEA-Nb and iHEA samples also show relatively high MUD in the <110> texture along the building direction (*Z*). Generally, it is known that the fcc crystal structure tends to grow in the preferred <001> orientation along the solidification direction during fusion-based additive manufacturing processes [36–38]. However, when the scanning strategy between the two consecutive layers is rotated to a certain degree, the preferred orientation and intensity can be changed to some extent. Specifically, during the LMD process, the molten pool is continuously solidified along the laser trajectory with the grains mainly growing along the <001> preferred orientation [36, 37]. Due to the semi-elliptical shape of the molten pool, the latent heat is also radially transferred from the laser scanning center to the boundaries of the molten pool, causing the grains with <001> orientation to grow mostly along 0° and 45° with respect to the building direction [39]. This ensures the grains of the current scanning layer and the previously solidified grains maintain preferential growth in the direction with the largest temperature gradient [37, 40]. However, due to the 180° angle rotation between every two consecutive layers in this study, the growth of crystal grains along 0° from the bottom of the molten pool would be suppressed. Meanwhile, along the laser scanning direction (*X*), the preferred <001> orientation is also interrupted by the bidirectional scanning strategy, which is replaced by the formation of <111> oriented grains. This is considered to be because the formation of <111> grains can be energetically favorable due to the arrangement of atoms in these close-packed directions. Therefore, most of the solidified crystals from the molten pool boundaries would grow at 45° from the building direction, coupled with the influence of the bidirectional scanning strategy, resulting in not only the <110> texture generated in the *Z* direction but also the strong <111> texture generated in the *X* direction. Generally, <111> and <110> orientations can lead to a better combination of strength and ductility than the <100> orientation in fcc-based metallic materials [7, 41] since deformation twinning is more favorable when <111> and <110> are along the tensile direction [42]. Thus, the current LMD-built iHEA-Nb sample is expected to have superior mechanical properties.

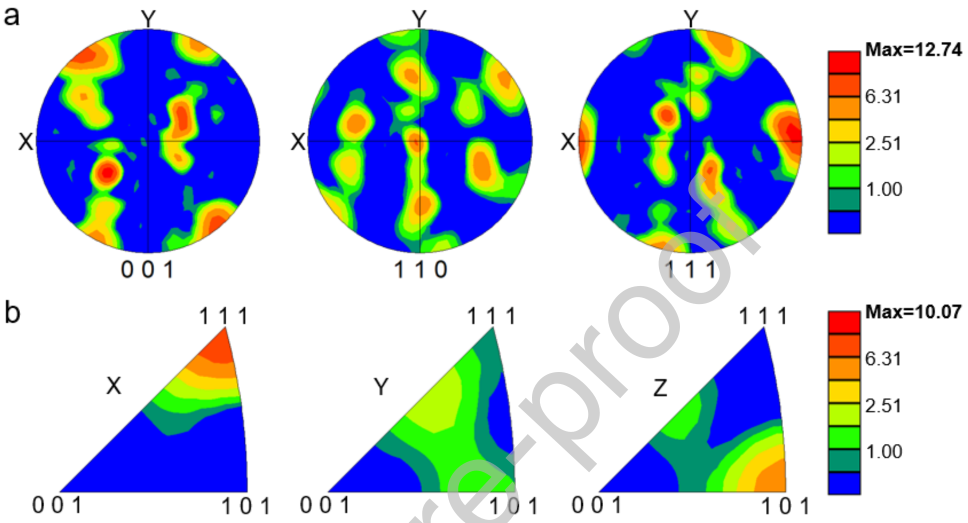

Fig. 2. (a) Pole figures (PFs) and (b) IPFs in the *XOY* plane.

The backscattered electron (BSE) image of the cellular sub-structures is shown in Fig. 3(a), which are commonly obtained in laser additively manufactured metallic materials [14, 17, 29, 43, 44]. According to the literature [29, 44], due to the rapid solidification of the additive manufacturing process, there is nearly 2% linear thermal strain remaining in the sample, contributing to a large number of dislocations within the as-built microstructure. As a result, cellular sub-structures were formed by the rearrangement of these remaining dislocations as well as dislocation entanglements during the layer-by-layer deposition process. This microstructural feature is generally considered a heterogeneous dislocation distribution due to the higher density dislocation at cellular boundaries compared to the cellular interiors. A high-magnification image of the cellular sub-structures with the corresponding EDS elemental mappings is shown in Fig. 3(b). According to the EDS mappings, a third type of heterogeneity, that developed in the as-deposited microstructure, arises from the segregation of alloying elements near cellular boundaries, which is attributed to different diffusivity and solubility capabilities of different elements in the matrix. A higher concentration of Mn element was detected at cellular boundaries, which could be explained by the solidification route of the current HEA. Specifically, during the rapid solidification of LMD-built components, elements with lower melting points (Mn: 1519 K in the current alloy compared to Fe: 1811 K, Co: 1768 K, Cr: 2180 K, and Nb: 2750 K) would segregate at the cellular boundaries due to the later start of the solidification process [29, 45]. Co and Cr elements remain almost uniformly distributed throughout the whole mapping region, while Fe is depleted along the subgrain boundaries. Similar results have also been observed by other researchers regarding the depletion of Fe and uniform distribution of Co despite their similar melting points, such as laser additively manufactured $(FeCoNi)_{85.84}Al_{7.07}Ti_{7.09}$ [46], $Fe_{47}Mn_{30}Cr_{10}Co_{10}Ni_{3}$ [47], and $Fe_{65}Ni_{15}Co_{8}Mn_{8}Ti_{3}Si$ HEA [29]. It is speculated that this heterogeneity in microscopic element distribution is mainly due to the higher solid solubility of Fe element in the current fcc matrix relative to Co, thus showing enrichment within subgrains and depletion at cellular boundaries. Nevertheless, detailed microstructural analysis and computational modeling are still required to fully understand this phenomenon, which is beyond the scope of this work.

Furthermore, the SEM-EDS results in Fig. 3(b) also show the distribution of Nb-rich particles with a bright contrast in the subgrain boundaries. To further analyze the elemental distribution of this bright white phase, the enlarged area of the cellular boundary including different precipitates in Fig. 3(b) is analyzed by EDS mapping, and the results are shown in Fig. 4. It can be observed that the content of Nb and C is higher in the bright white phase, which is most likely NbC carbides that will be verified in the following analysis. It can be speculated that only a small amount of Nb is dissolved into the fcc matrix phase during the LMD alloying process, while the remaining Nb gives rise to the formation of Nb-rich carbides.

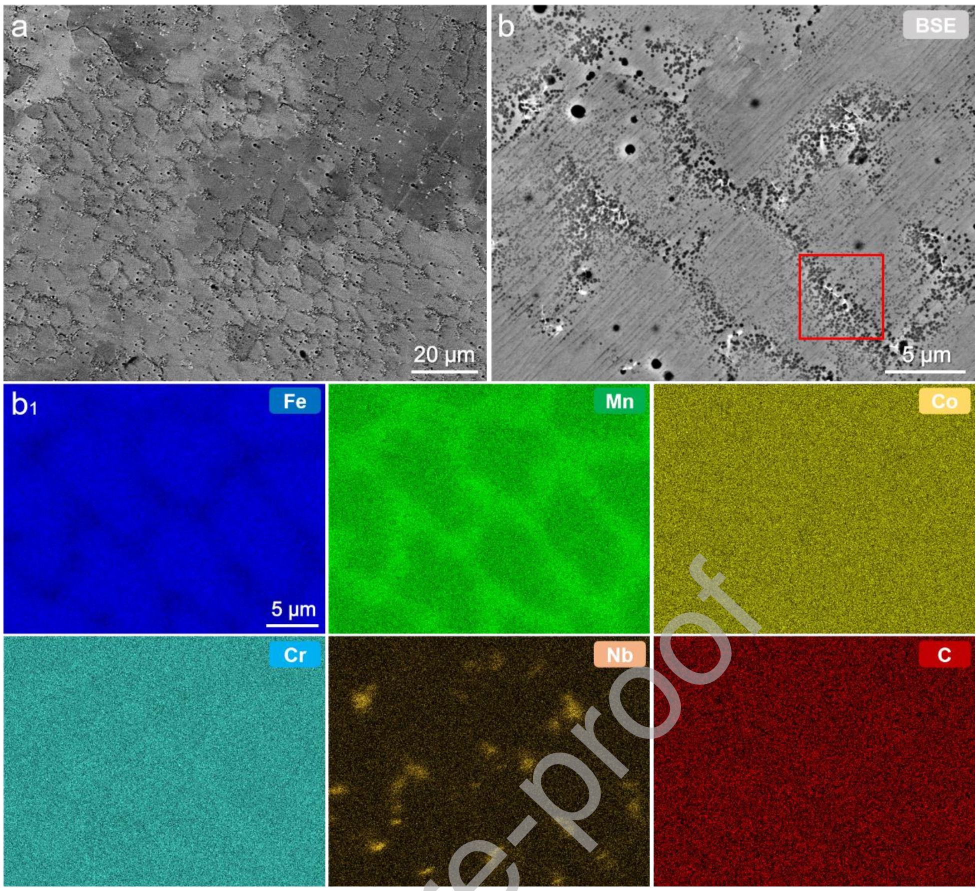

Fig. 3. (a) BSE image of the cellular sub-structures for the iHEA-Nb sample. (b) High-magnification BSE image of the cellular sub-structure with the corresponding EDS elemental mappings in (b_1).

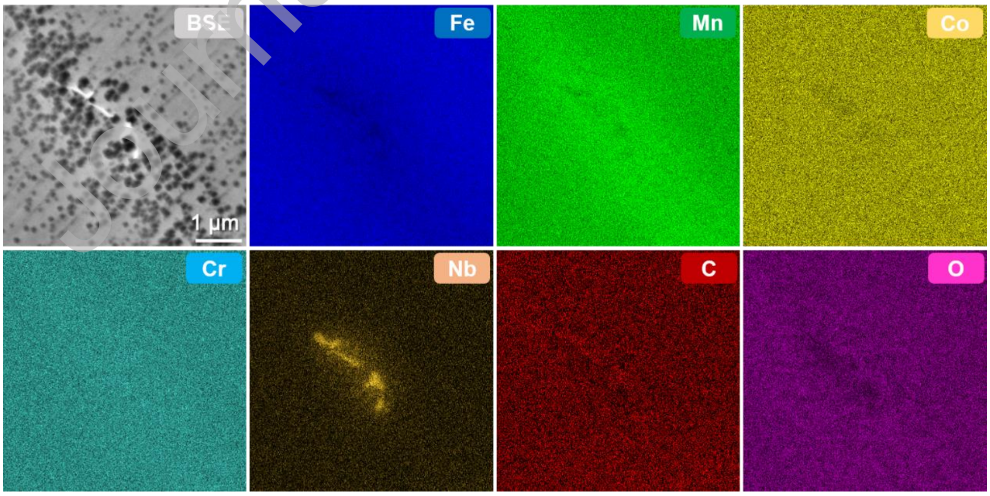

Fig. 4. SEM image and EDS elemental mapping of the marked area at the cellular boundary in Fig. 3(b).

The phase constituents for the LMD-built iHEA-Nb sample were identified by high-energy SXRD analysis, as shown in Fig. 5. The diffraction pattern is indexed to a four-phase composition, including the predominant fcc phase, and NbC, $M_{23}C_6$, M_7C_3 carbides, with phase fractions of 97.42%, 0.85%, 1.03%, and 0.66%, respectively. It should be noted that this high-energy synchrotron technique is known for its high spatial resolution (at the nanometer scale) [48], which coupled with the high signal-to-noise ratio allows to detect nanoscale phases even with low phase fractions as in the case of the present carbide precipitates. When using conventional laboratorial X-ray diffraction measurements, the diffraction peaks associated with these phases are hidden in the background. The lattice constants of the fcc phase obtained were calculated to be 3.353 Å and 3.355 Å for the iHEA and iHEA-Nb, respectively, indicating that the lattice constant increases after adding Nb. The solid solution of Nb with a relatively larger atomic radius will cause lattice distortion and generate a lattice stress field [49], which can increase the lattice parameter of the fcc matrix and also increase the resistance to dislocation movement. It is worth noting that the currently obtained lattice parameters of fcc solid solutions are significantly different from the reported data (~3.62 Å of similar alloys reported in [50]). This is thought to be related to the different thermal cycles and heat treatments the materials experienced during different processes, despite being similar in composition. Tong et al. [51] have reported that after heat treatment, the lattice parameters of LAMed FeCrCoMnNi HEA are generally larger than those of as-built samples. Similar conclusions were also reported in [52]. Besides, the high laser power is believed to also have contributed to the reduced lattice parameters due to the aggravated volatilization of the Mn element [51]. The currently detected NbC carbides with a cubic crystal structure are consistent with the Nb- and C-rich precipitated phase detected by EDS analysis in Fig. 4, as well as previous reports on the formation of Nb-rich MC carbides in Nb-added HEAs [53, 54]. According to [55], the trace element Nb has a strong affinity for C, which can form a stable NbC phase and refine the fcc matrix. In addition, due to the high mismatch (25%) between NbC and the fcc matrix, it is more difficult for NbC to nucleate and precipitate in the fcc matrix, which would generally precipitate from crystal defects such as grain boundaries and dislocations [56], thus reducing the distortion energy caused by nucleation. The formation of $M_{23}C_6$ and M_7C_3 carbides was also detected for this iHEA without Nb addition (Fig. S4). In Li et al.'s work [12], the chemical composition of this $M_{23}C_6$ precipitate was detected as 47.16 Cr, 17.82 Mn, 13.64 Fe, 1.92 Co, and 19.46 C (at.%) by atom probe tomography. The generation of different carbides at grain boundaries in the current iHEA-Nb sample would hinder the grain boundary mobility and avoid the excessive grain growth of the original fcc phase due to the pinning effect, resulting in the formation of more fine grains near the laser tracks and layer interfaces shown in Fig. 1.

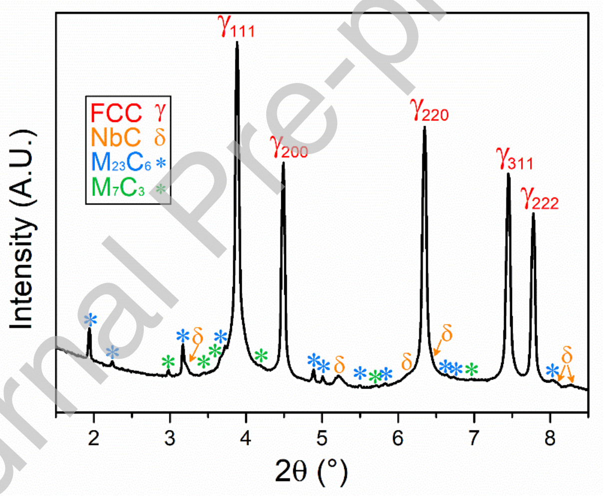

Fig. 5. SXRD pattern of the LMD-built iHEA-Nb sample.

TEM analysis was performed to elucidate the nanoscale microstructural features of the as-deposited iHEA-Nb for further investigation of the formation of precipitates and dislocation networks. Fig. 6(a) shows the overall bright-field STEM image of one lamella, with the diffraction spots in Fig. 6(b) indicating a single-phase fcc structure of the matrix. High-density dislocations could be observed in this TEM lamella (Fig. 6(a, c)), resulting from the thermal contraction strain to accommodate the solidification shrinkage stress during rapid cooling [7, 57]. Under the same laser processing conditions, the dislocation density in the iHEA-Nb sample is higher than that of the reference iHEA sample (Fig. S5), with the values of 3.97×10^{14} and 2.21×10^{14} mm^{-2}, respectively, which were calculated from the SXRD results according to the Williamson-Hall method [58]. The relatively higher dislocation density in the iHEA-Nb sample is mainly attributed to the following two reasons: (i) The hindering effect of Nb-containing particles to dislocations caused dislocation entanglement and increased dislocation density; (ii) Extra dislocations induced by the discrepancy in the coefficient of thermal expansion between Nb-containing particles and the fcc matrix. Accordingly, the cooling from solidification would lead to high localized stress around the particles [59–61]. These stresses can induce additional defects such as dislocations, thereby increasing the dislocation density. Fig. 6(c) shows enlarged images of three circular precipitates with different sizes in Fig. 6(a), where dislocation entanglements were detected around these precipitates. The EDS elemental mappings in Fig. 6(d) reveal that these precipitates are Mn-rich oxides, which were also detected in Nb-free iHEA samples [27]. The local enrichment of O is, on the one hand, considered to be related to the contamination during the powder fabrication process, and on the other hand, is considered to be due to the current LMD process where the Ar gas shielding was insufficient to fully protect the melt pool from oxygen.

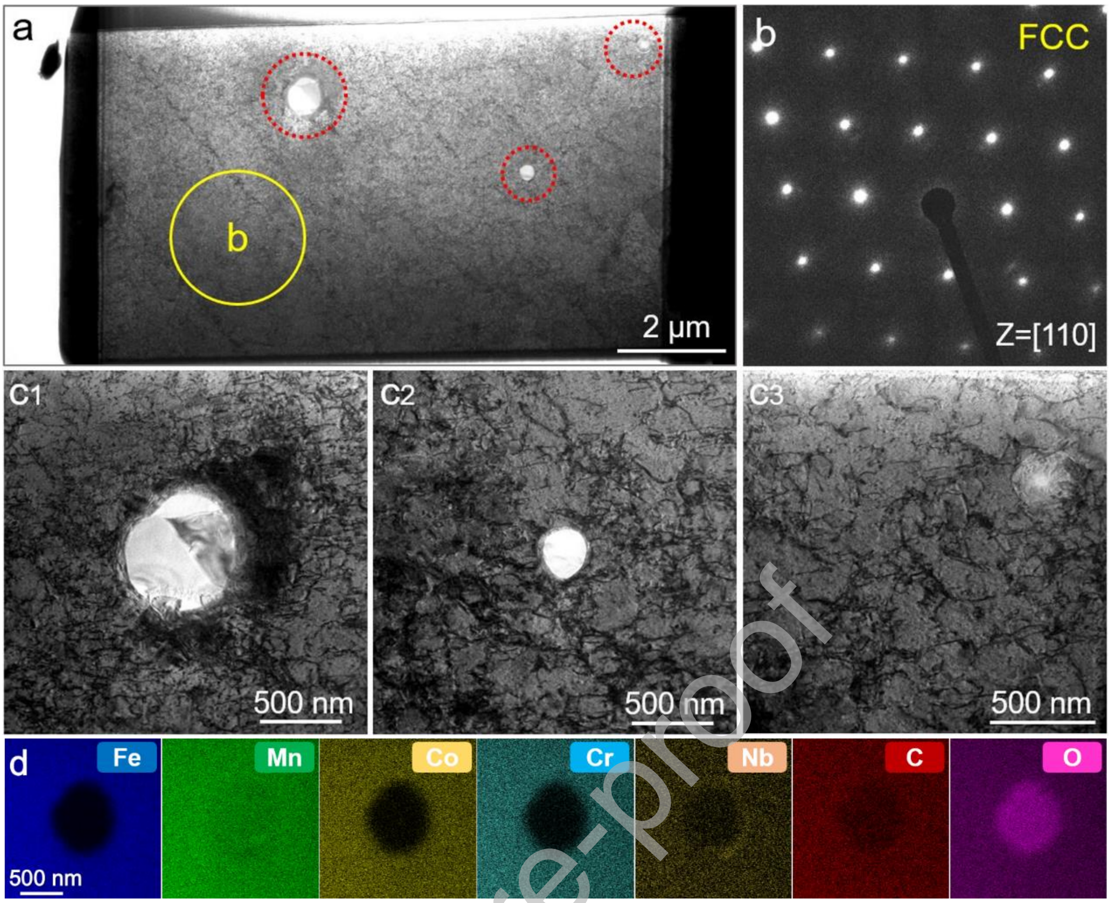

Fig. 6. TEM results of the LMD-built iHEA-Nb sample. (a) Overall bright-field STEM image, (b) SAED pattern from the area marked in (a), (c) enlarged images of circular precipitates with different sizes, and (d) EDS elemental mapping of the precipitate in (c1).

Different carbides were also observed by TEM. Fig. 7(a) shows a large number of nanoscale $M_{23}C_6$/M_7C_3 precipitates distributed within the fcc matrix, as indicated by the red arrows. Fig. 7(b) is the corresponding dark-field image, revealing the entanglement effect of these carbides on dislocations. However, due to their smaller size, $M_{23}C_6$/M_7C_3 carbides do not cause the accumulation of large dislocations as those oxides do. The moiré pattern within the TEM image can be identified in the enlarged image of the $M_{23}C_6$/M_7C_3 precipitated particles in Fig. 7(c). Moiré patterns or fringes are produced when two similar patterns are overlapped with different spacings or orientations [62]. Here, in the current nanostructure, the moiré fringes are due to the overlapping of two different phases, namely the fcc matrix and $M_{23}C_6$/M_7C_3 carbides, with different lattice spacings at the interface [62–64]. The corresponding diffraction spots are shown in the inset in Fig. 7(c). It has been reported that the formation of M_7C_3 carbides involves uphill diffusion of alloying elements, most importantly Cr [65, 66]. During the cooling of the alloy from the stable field of single-phase fcc austenite, the formation of M_7C_3 carbides precedes the formation of $M_{23}C_6$ carbides [67]. As the temperature decreases, the thermodynamic stability of M_7C_3 decreases at the expense of $M_{23}C_6$ [67, 68]. Any pre-existing M_7C_3 can transform to $M_{23}C_6$ or aid its nucleation [66]. Therefore, these carbide precipitates can be a mix of M_7C_3 and $M_{23}C_6$ [66], which is also considered suitable for the current nanostructure due to the trace contents of both carbides (1.03% and 0.66% for $M_{23}C_6$ and M_7C_3, respectively), where $M_{23}C_6$ accounts for the majority. The crystal structure of $M_{23}C_6$ carbide is similar to that of fcc austenite (Fm3m space group). According to the previous research [69–71], $M_{23}C_6$ carbides and the fcc austenite matrix usually maintain a parallel orientation, showing a cube-on-cube orientation relationship ($(111)\gamma//(111)M_{23}C_6$, $[110]\gamma//[110]M_{23}C_6$); therefore the carbide diffraction spots shown in the insert of Fig. 7(c) are parallel to the fcc matrix. The indexed lattice parameter of $M_{23}C_6$ carbides is 1.066 nm, which is consistent with the results of reference [66] and is almost three times the current fcc lattice parameter (~0.355 nm). The high-resolution TEM (HRTEM) image in Fig. 7(d) also shows that it is semi-coherent with the fcc matrix.

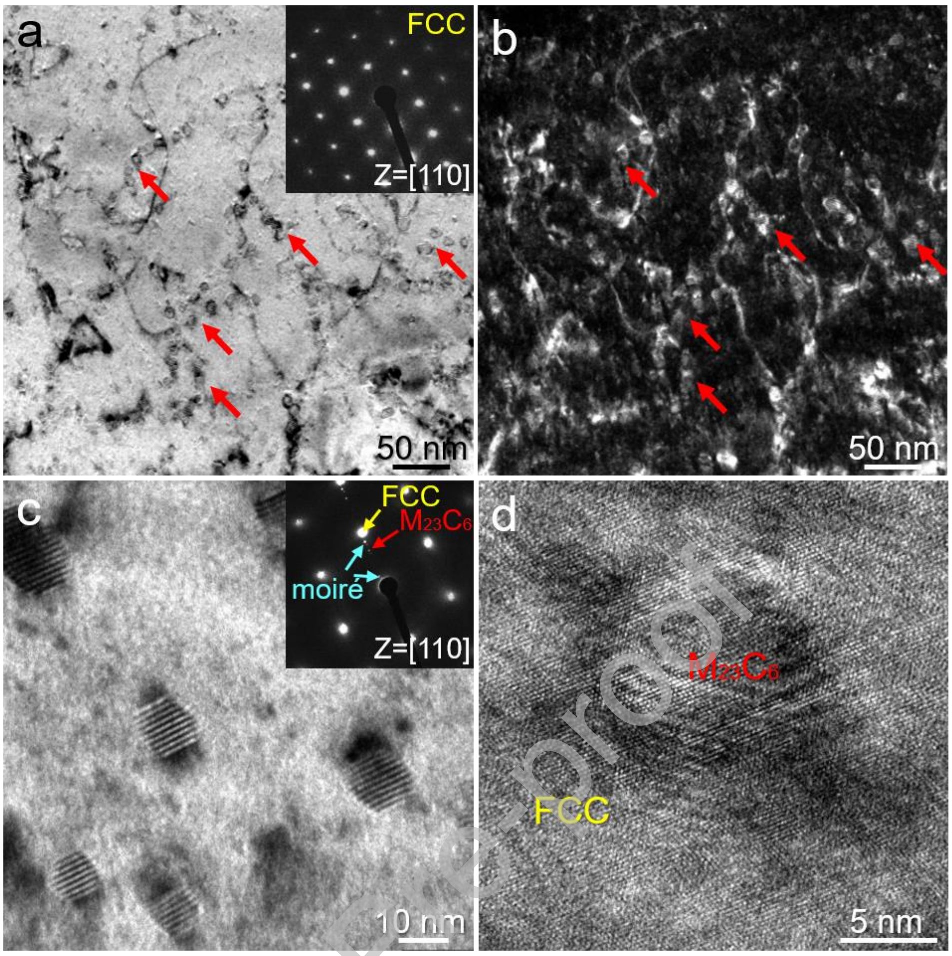

Fig. 7. (a) Bright-field TEM image of the $M_{23}C_6/M_7C_3$ carbides within the fcc matrix and (b) the corresponding dark-field image. (c) Enlarged image of the $M_{23}C_6/M_7C_3$ carbides showing the Moiré patterns, (d) HRTEM image of the carbide showing the semi-coherent interface.

In order to characterize the nanostructure of Nb-rich carbides, the cellular boundary containing Nb-rich particles was selected to prepare TEM lamella. Fig. 8(a) shows the bright-field TEM image in which the Nb-rich precipitated phase is marked with a blue arrow. Fig. 8(b) is an enlarged image of the Nb-rich phase. Moiré fringes can be seen at the interface between the Nb-rich phase and the fcc matrix, similar to those previously observed for $M_{23}C_6/M_7C_3$ carbides. The corresponding diffraction patterns (Fig. 8(c)) obtained from the Nb-rich precipitate phase were indexed as fcc structure with a lattice parameter of 0.425 nm, close to

NbC carbides with the lattice parameter of 0.44 nm [72]. Combining SEM-EDS and high-energy SXRD analysis, this Nb-rich phase is revealed to be NbC carbide.

The present diffraction patterns indicate that NbC also exhibits a cube-on-cube orientation relationship with the fcc matrix, which was also reported in [73, 74]. This orientation relationship is again verified by the HRTEM image in Fig. 8(d), where the two crystal structures are semi-coherent. Compared to the incoherent boundaries, the coherent ones can promote the diffusion of the elements [75, 76], e.g., Nb and C, so the NbC precipitates are easier to precipitate in the current Nb-added iHEA. NbC would inhibit the movement of dislocations and improve the strength and toughness of the material. However, an excessive NbC phase would also destroy the continuity of the matrix, leading to a decrease in the material properties [55].

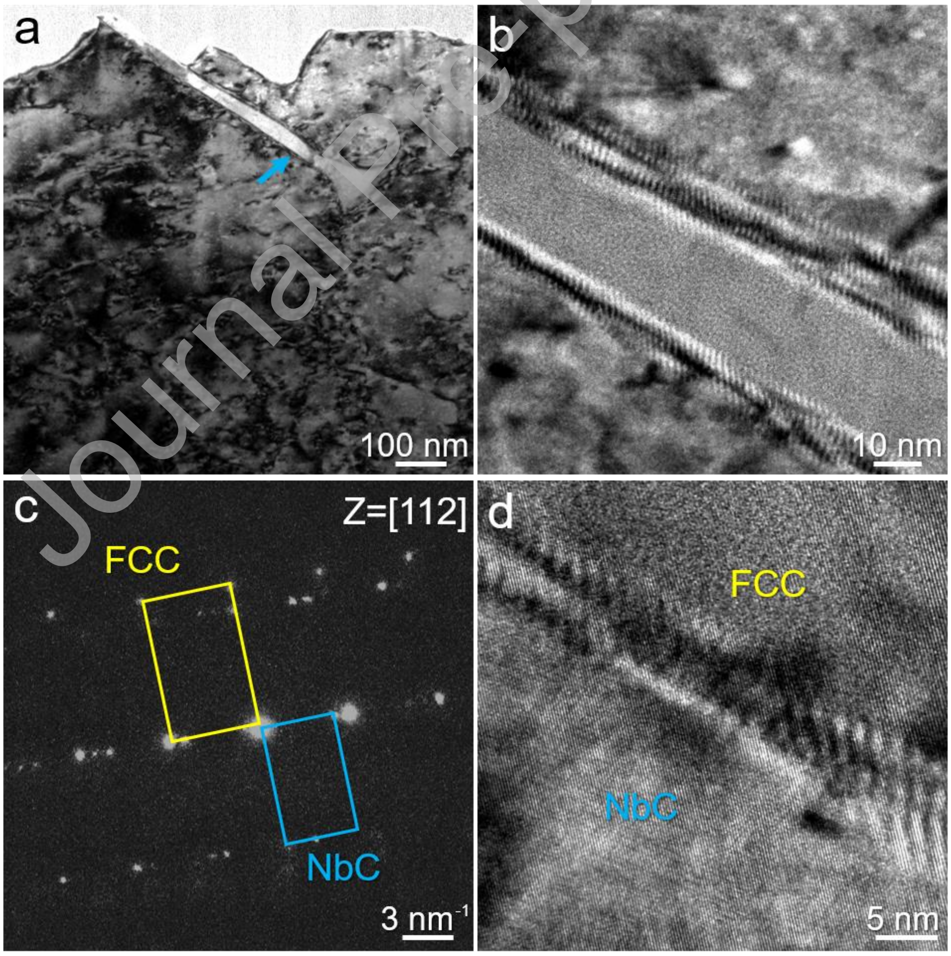

Fig. 8. (a) Bright-field TEM image of the Nb-rich phase within the fcc matrix, (b) enlarged image of the Nb-rich phase showing the Moiré patterns with the matrix, and (c) the corresponding diffraction patterns revealing the phase of NbC carbides. (d) HRTEM image showing the semi-coherent interface between NbC and the fcc matrix.

3.2. Tensile test and deformation characteristics

Representative engineering stress-strain curves of the LMD-built iHEA-Nb and reference iHEA samples are shown in Fig. 9(a). Despite the relatively coarse microstructure, the as-deposited iHEA-Nb sample presented superior yield strength (YS) and significantly improved ultimate tensile strength (UTS) of 1140 and 1450 MPa, respectively. Compared to the iHEA without Nb addition this is an increase of 44% and 45% in YS and UTS, respectively. Although this enhancement in mechanical strength is at the expense of a slightly decreased total elongation compared to the iHEA sample, the obtained elongation value still remains in an acceptable range above 30%. These results clearly demonstrate that the Nb addition in the iHEA sample *in situ* improved the mechanical properties while avoiding the strength-ductility trade-off. The high dislocation density in the form of subgrain boundaries, along with dislocation entanglements around the precipitates, allows for high strain hardenability to resist early necking, resulting in a high tensile strength [77]. The slightly decreased ductility can be explained by typical plastic instability and strain localization around the increased density of precipitates of the current iHEA-Nb sample [78, 79].

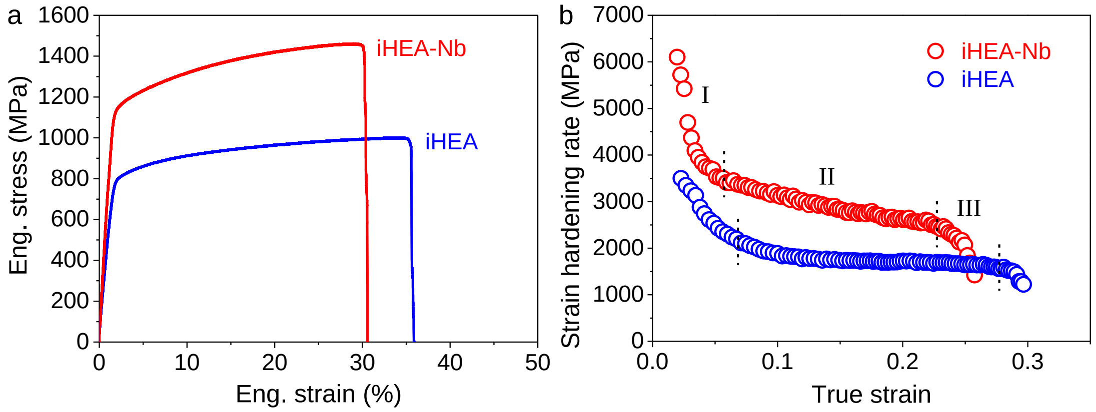

Fig. 9. (a) Engineering stress-strain and (b) work hardening rate curves of the LMD-deposited iHEA-Nb and iHEA tensile samples.

Fig. 9(b) shows the corresponding strain hardening rate (SHR) curves. The SHR curve in both samples shows three distinctive stages. Stage I for both samples consists of a sharp drop in SHR value after yielding to ~5%–6% true strain due to dynamic recovery-induced strain softening, and dislocation slip is acting as the primary deformation mechanism at this stage [29, 80]. Thereafter, stage II exhibits slightly different trends in these two alloys, characterized by a near-stabilized SHR plateau for the iHEA sample and a gradually decreasing SHR for the iHEA-Nb sample. By comparison, the iHEA-Nb alloy exhibits a remarkably higher SHR in this stage, attributed to the enhanced effects of solid solution strengthening and precipitation strengthening, which results in more dislocations successively proliferating and entangling with each other. In stage Ш, the SHR of both samples decreases until failure occurs.

Additively manufactured metallic materials usually have heterogeneous microstructures on the scale of several nanometers to hundreds of micrometers, and strain partitioning during deformation necessitates the presence of geometrically necessary dislocations (GNDs) to maintain interface compatibility between this heterogeneous microstructure. In other words, the accumulation of GNDs near boundaries, such as grain boundaries, twin boundaries, phase boundaries, etc., compensates for the plastic incompatibility at the interface between different regions [81]. These GNDs generate significant back stress during plastic deformation to suppress the movement of dislocations [7], accelerating the strain-hardening rate of heterogeneous structural materials. Furthermore, at the nanoscale, the formation of nano-precipitates can also impede dislocation motion during plastic deformation by acting as a direct pinning agent, thus forming profuse GNDs and effectively generating high back stress. The current LMD-built iHEA-Nb samples have sub-structures and precipitates decorated with dislocations, which can provide stable barriers against dislocation motion for strengthening, while simultaneously ensuring a continuous plastic flow by accommodating dislocations from transmitting [7, 57]. It can therefore be deduced that the large number of sub-structures and high carbide fractions in the as-built iHEA-Nb sample is favorable to induce high back stress strengthening and contribute to the high strain hardening capability upon deformation of the current material. It is worth mentioning that Mn segregation at sub-grain boundaries (Fig. 3) can misfit with the fcc matrix and cause lattice distortion, which may also hamper dislocation movement during deformation, thus yielding a higher SHR [7, 18].

A comparison of the mechanical responses of different classes of as-printed HEAs produced using different additive manufacturing methods including LMD [16, 18, 82–86], selective laser melting (SLM) [7, 87–92], selective electron beam melting (SEBM) [93–96] and wire arc additive manufacturing (WAAM) [97], with the work presented here is provided in Fig. 10. This comparison reveals that the Nb alloying design leads to the extraordinary strength-ductility synergy of the current iHEA-Nb at room temperature, which stands out from most of the usual strength-ductility trade-off HEAs and pushes the paradigm for the tensile properties of additively manufactured HEAs.

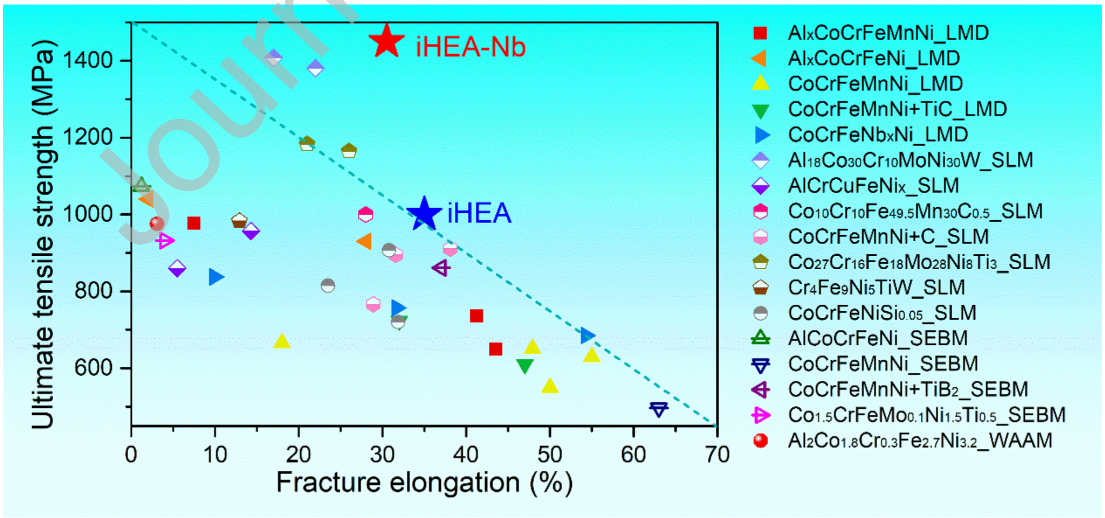

Fig. 10. Comparison in UTS and elongation of HEAs produced by different additive manufacturing techniques [7, 16, 18, 82–97].

Figs. 11 and 12 illustrate the orientation distribution function (ODF) at φ_2 = 45° section and IPF texture of the tensile samples before and after deformation of the iHEA-Nb and Nb-free reference samples, respectively. The IPFs show the orientation of the grains with respect to the tensile direction (TD) as a reference axis. The main texture components of the samples described in {hkl} parallel to the tensile plane (*XOY*) and <*uvw*> and the main fiber parallel to the TD are presented in Table 1. Fig. 11(a, b) illustrates the texture components of the iHEA-Nb samples before deformation, which shows a similar structural texture to that of Nb-free iHEA tensile sample with the fiber texture of <111> // TD orientation (Fig. 12(a, b) [27]). After the fracture, no considerable change is observed for the Nb-added sample as the main texture components of A and Copper with the fiber of <111> // TD remain intact after the tensile test. In comparison, the Nb-free iHEA sample after fracture also shows the main A texture component with the fiber texture <111> // TD. However, the Copper texture component in the iHEA reference sample before deformation disappears, and instead a minor Goss texture emerges during deformation (Fig. 12(c)). The IPF of the deformed iHEA sample in Fig. 12(d) confirms that the main fiber texture of <111> // TD is retained after fracture, and it is now combined with a minor fiber texture of <001> // TD related to the Goss texture.

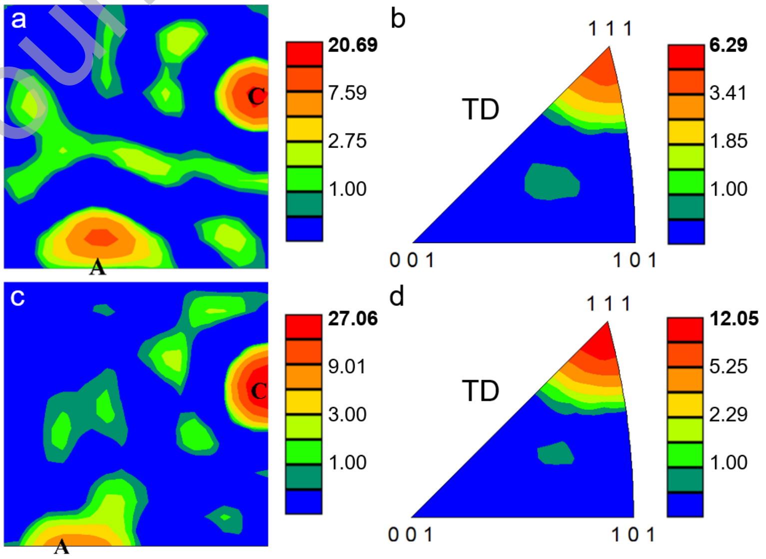

Fig. 11. φ_2 = 45° ODF sections and IPF texture of iHEA-Nb tensile samples with respect to the TD reference axis (a, b) before and (c, d) after tensile deformation.

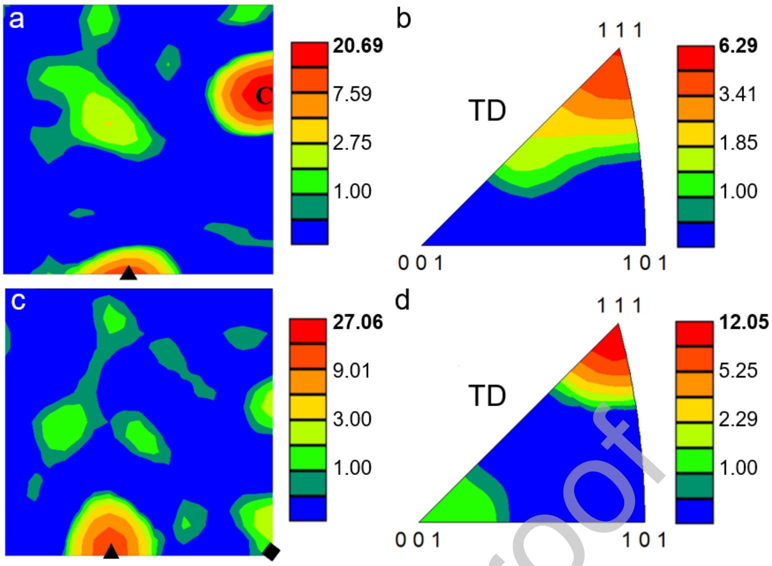

Fig. 12. φ_2 = 45° ODF sections and IPF texture of Nb-free reference samples with respect to the TD reference axis (a, b) before and (c, d) after tensile deformation [27].

Table 1 Main texture components in {*hkl*}<*uvw*> notations and the corresponding fiber texture.

Symbol	Texture component	{*hkl*}<*uwv*>	Fiber
▲	A	{110}<1–11>	<111> // TD
C	Copper	{112}<–1–11>	<111> // TD
◆	Goss	{110}<001>	<001> // TD

Fig. 13 shows EBSD results of the tensile deformed microstructure of the iHEA-Nb and Nb-free iHEA sample near fracture with an overall engineering strain of ~30% and ~35%, respectively. White lines in Fig. 13(b) highlight the twin boundaries (TBs) with 60° misorientation around <111>. Both iHEA and iHEA-Nb tensile samples have a similar initial texture with a strong fiber texture of <111> // TD. However, after deformation, the iHEA-Nb shows a smaller volume fraction of mechanical twins compared to the reference iHEA sample shown in Fig. 13(c, d). There is also a drastic reduction in the thickness of the twins formed in the deformed iHEA-Nb sample. Similar results were also reported for the Nb-micro alloyed TWIP steels [98, 99]. Yen et al. [100] reported that the VC carbides in TWIP steel expose retarding force to the twinning dislocations once they encounter carbides. Since the twinning dislocations are not able to shear the hard carbides, they wind around the carbides and an untwined area is formed. As a result, the <001> // TD fiber texture obtained in the case of the deformed Nb-free iHEA sample (Fig. 12(d)) is not observed in the failed iHEA-Nb sample due to the lower density of mechanical twins.

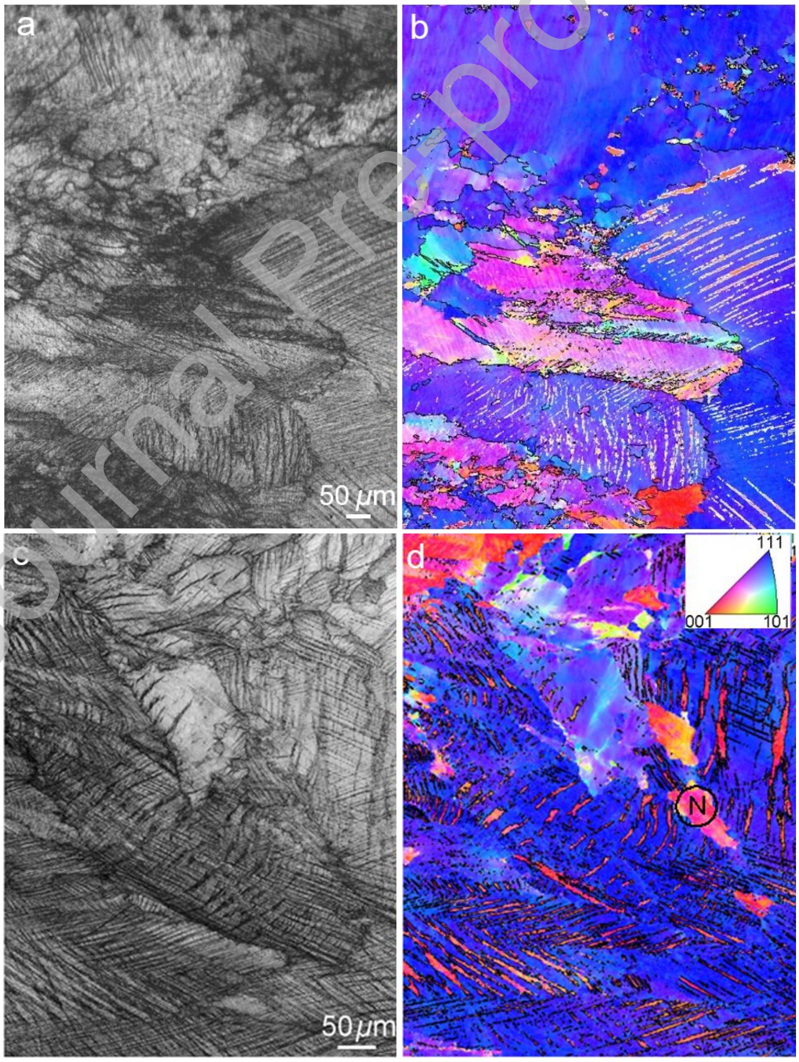

Fig. 13. (a) Image quality and (b) IPF maps of the iHEA-Nb sample after tensile deformation, (c, d) The corresponding images of the Nb-free reference sample [27].

In addition to the suppression of deformation twins by carbides, the direct effect of Nb addition on the stacking fault energy (SFE) of the current HEA system also needs to be considered. In general, the effect of alloying elements on SFE can vary depending on the specific alloy composition, processing conditions, and heat treatment methods. In many cases, the addition of Nb can lead to an increase in the SFE of the fcc matrix, especially in the alloys of low Ni content [101]. This is because Nb is known to strengthen the matrix by forming solid solutions or precipitates. The stronger the matrix, the higher the energy required to nucleate and move stacking faults, resulting in an increase in SFE. Ishida [102] has found that alloying of Fe-18Cr-10Ni austenitic stainless steel alloyed with 1% Nb increases the SFE through thermodynamic analysis. Vitos et al. [103] also obtained a similar conclusion using quantum-mechanical first-principles calculations, that is, adding Nb to $Fe_{65.5}Cr_{17.5}Ni_{12}Nb_5$ quaternary austenitic stainless steel increased the overall SFE. In [104], the authors found that increasing the Nb content from 0.0 to 3.0 atomic percent increased the ISFE of fcc austenitic Fe from –89.32 to –25.8 mJ m^{-2}. From the structural energy difference and thermodynamic perspectives, these results indicate that the Nb element stabilizes the fcc phase relative to the hcp phase. It is also important to mention that changes in SFE can affect the preferred deformation mechanism of the material. Increased SFE can shift the deformation mode from twinning to slip. Bai et al. [55] used the Olson-Cohen thermodynamic model to calculate that the SFE of Fe-25Mn-9Al-8Ni-1C-*x*Nb alloy increased from 18 to 55 mJ m^{-2} as the Nb content increased. Within this SFE range, although the twinning-induced plastic deformation mechanism was still dominant, strain-induced twinning was delayed to a certain extent with increasing Nb content [105]. Moreover, in addition to SFE, deformation twins are also affected by other parameters such as grain size [106–109]. Studies have shown that grain refinement can suppress the twinning-induced plastic deformation behavior [107–109].

To sum up, we believe that in the current Ni-free iHEA alloy system, the addition of Nb leads to the decrease in mechanical twin density in the sample for three main reasons: (i) the increase in SFE, (ii) retarding force by the carbides (inhibition effect of carbides), and (iii) grain refinement.

Additionally, Nb addition can also increase the dislocation density, as observed in Fig. 6 and also verified by SXRD calculations. Higher dislocation density combined with enhanced solid solution hardening as well as the formation of NbC carbides can contribute to the higher strength and SHR of the current iHEA-Nb sample, as shown in Fig. 9. Furthermore, it is well known that the formation of deformation twins contributes to the high SHR in HEAs [110]. The continuous decrease in SHR (stage II) of the iHEA-Nb sample (Fig. 9(b)) can thus be attributed to suppressed or limited mechanical twin formation compared to the Nb-free iHEA sample.

To further clarify the deformation characteristics of the as-built iHEA-Nb sample, TEM analysis was performed on FIB lamellas extracted from the fracture region with an overall engineering strain of ~30%. The overall bright-field STEM images in Fig. 14(a, b) from two FIB lamellas revealed the morphology of massive dislocation networks between the striped structures in the deformed fcc grains. These stripe-like deformed structures were confirmed to be deformation twins (DTs) by transmission EBSD analysis in Fig. 14(c). Both primary and secondary twins were observed in the deformed iHEA-Nb sample. The corresponding HRTEM image and SAED pattern in Fig. 14(d, e) also confirm that the fcc spots show a typical Σ3 twin boundary symmetry, indicating the formation of such twin substructures within the fcc matrix. In addition to hindering the movement of dislocations, the continuous nucleation of deformation-induced twins also shortens the mean free path of moving dislocations, thus improving the dislocation storage and strain hardening capability of the alloys [29, 111]. Furthermore, stacking faults (SFs) can also be developed in the fcc matrix to accommodate the applied strain, as illustrated in the bright-field STEM image in Fig. 14(f). As indicated by the yellow arrows, multiple straight lines with differing contrast fringes were observed in the fcc matrix, indicating the formation of SFs through the motion of partial dislocations, which typically occur during the deformation of materials with low stacking fault energy [29].

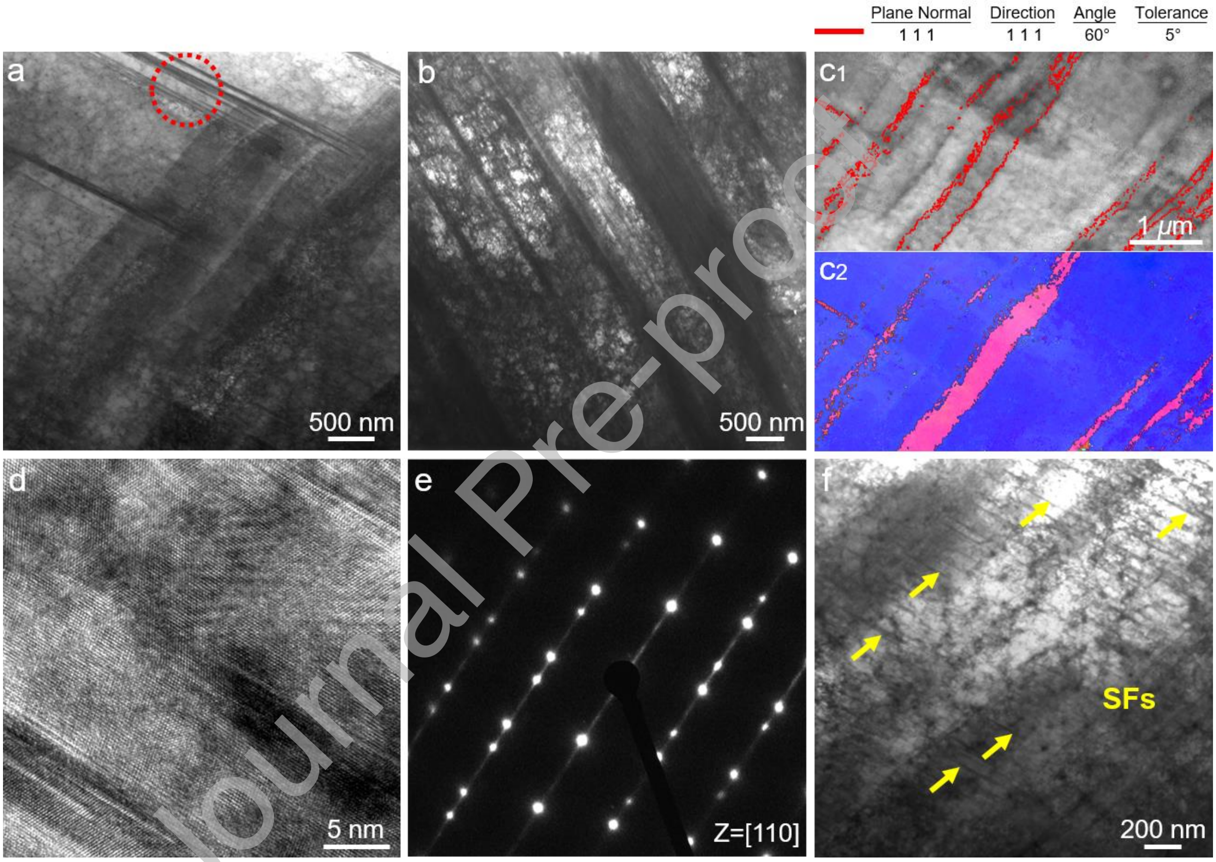

Fig. 14. (S)TEM results of iHEA-Nb sample after tensile deformation. (a, b) Overall bright-field STEM images from two FIB-produced lamellas, (c) image quality and IPF maps by transmission EBSD analysis, (d) HRTEM image, and (e) the corresponding SAED pattern of the area marked in (a), (f) multiple stacking faults highlighted by the yellow arrows in the fcc matrix phase.

Additionally, various precipitates also play an important role in the deformation process. TEM was utilized to investigate the interaction between different precipitates and dislocations on thin lamellae extracted from the tensile deformed area near the fracture, and the results are shown in Fig. 15. The bright-field TEM image in Fig. 15(a) shows significant dislocation entanglements around the NbC carbide. In addition to the dislocation accumulation, a large number of $M_{23}C_6/M_7C_6$ nanoparticles (as indicated by the red arrows) can also be observed from the HRTEM image at the interface between NbC and the fcc matrix shown in Fig. 15(b). These results once again verify that the NbC precipitate phase formed in the current Nb-added sample plays a very important role in improving the strength of the sample. As for the hard $M_{23}C_6/M_7C_3$ carbides themselves, although they maintain a semi-coherent relationship with the fcc matrix (Fig. 7(d)), aggregation of dislocations can still be observed around them instead of being sheared by dislocations (Fig. 15(c)). However, their ability to hinder dislocation movement has been significantly reduced compared to the large-sized NbC carbides. Compared with the $M_{23}C_6/M_7C_3$ carbides in the as-deposited state, these nanoparticles remain undeformed after the passage of dislocations during tensile deformation, confirming the Orowan looping mechanism. However, their orientations have changed to varying degrees (Fig. 15(d)), resulting in the destruction of their cube-on-cube orientation relationship with the fcc matrix compared to the as-deposited state (Fig. 7(c)), which can also be observed from the HRTEM image in Fig. 15(e). Lastly, the Mn-rich oxide particles, appearing as bright circular shapes, remain largely undeformed as shown in Fig. 15(f). A large number of dislocations are accumulated around them, confirming the Orowan strengthening mechanism. Overall, different types of precipitates in the current LMD iHEA-Nb sample can be classified as impenetrable particles when interacting with mobile dislocations, which can act as obstacles against the motion of dislocations during deformation and result in further precipitation strengthening.

Tensile deformation of the iHEA-Nb sample involves that each component plays a specific role in strain accommodation. At the early stage of plastic deformation, the softer fcc matrix phase accommodates most of the applied strain. Then, a large number of dislocations are generated within the fcc phase as the strain level increases. When the stress exceeds a specific critical stress, deformation-induced twins subsequently nucleate in the fcc matrix due to strain localization, resulting in TWIP. The formation of SF planar defects also provides continuous strain hardening. Furthermore, various precipitates also promote precipitation strengthening through the Orowan strengthening mechanism during the deformation process. Meanwhile, the accumulation of dislocations around precipitates gives rise to the sustained boundary coherency [29], which can be considered the side effect of precipitation strengthening and leads to a slight decrease in elongation for the current iHEA-Nb sample.

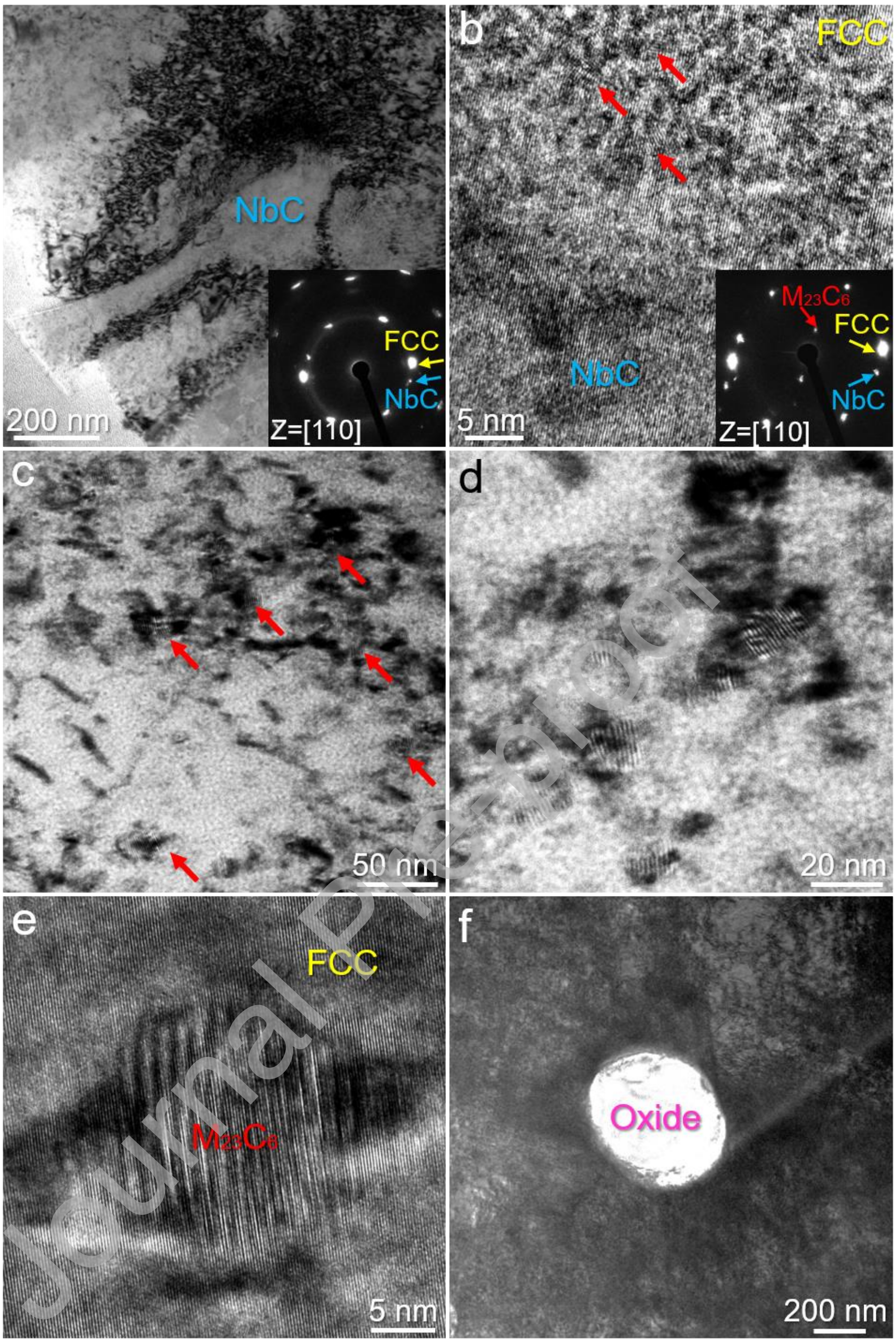

Fig. 15. (a) Bright-field TEM image showing significant dislocation entanglement around the NbC carbide, (b) HRTEM image of the interface between NbC and the fcc matrix. (c) Bright-field TEM image of $M_{23}C_6$/M_7C_3 carbides within the matrix showing the aggregation of dislocations, (d) enlarged image of the $M_{23}C_6$/M_7C_3 carbides after tensile deformation, (e) HRTEM image of the carbide showing interrupted semi-coherent interface with fcc matrix. (f) Mn-rich oxide particle in the deformation region.

3.3. Micropillar compression testing

The results of micropillar compression on the iHEA-Nb sample along [001] and [111] orientation, respectively, are presented in Fig. 16. The [001] iHEA-Nb micropillar shows similar fracture behavior with that of the [001] micropillar without Nb addition, exhibiting strain bursts and also unstable work hardening [27]. The micropillar is well-oriented for twinning but shows smaller strain bursts and stress drops (Fig. 16(a)) compared with the micropillar of the same orientation without Nb. It implies that mechanical twins are less activated in the iHEA-Nb micropillar. This can also be seen from the deformed [001] micropillar in Fig. 16(c), where narrower steps are formed. A continuous yielding and stable work hardening is observed for the iHEA-Nb micropillar along the [111] axis that is deformed via slip. As summarized in Table 2, Nb addition enhances the yield onset and also the critical resolved shear stress (CRSS) for both twining and slip. The $\mathrm{WHR}_{\mathrm{y}\rightarrow 10\%}$ also increases after Nb addition. Although no Nb-added tensile sample along <001> // TD was tested in this work, the micropillar compression results indicate a profound effect of Nb on the tensile sample deformed via slip. Therefore, it can be concluded that Nb addition retards the formation of twins and at the same time increases the strength and work hardening of the as-built structure by hampering slip.

Table 2 Summary of the micropillar compression test results.

Pillar	Deformation mode	Yield strength, σ_{y} (MPa)	CRSS for slip, τ_{slip} (MPa)	CRSS for twin, τ_{twin} (MPa)	$\mathrm{WHR}_{\mathrm{y}\rightarrow 10\%}$ (MPa)	Refs.
[001]	Twin	625 ± 70		290 ± 38	2091	[27]
[111]	Multiple slip	563 ± 98	148 ± 45		4198	[27]
[001]-Nb	Twin	690 ± 85		325 ± 61	2986	present

[111]-Nb	Multiple slip	823 ± 69	236 ± 65		6219	present

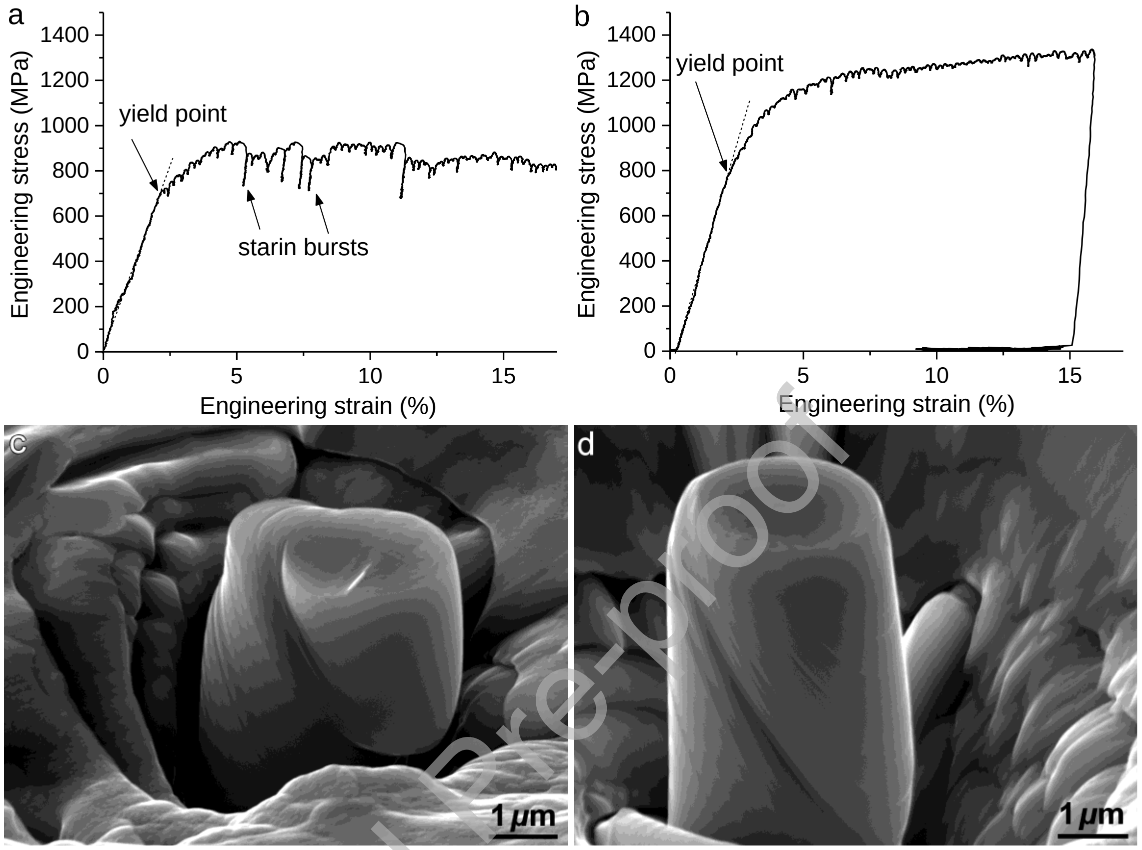

Fig. 16. Stress-strain curves of the iHEA-Nb micropillar compression test along (a) [001] and (b) [111] orientations, (c, d) The corresponding SEM images of deformed micropillars.

4. Conclusions

In summary, this study successfully fabricated Nb-added $Fe_{49.5}Mn_{30}Cr_{10}Co_{10}C_{0.5}$ iHEA using the laser melting deposition method. The microstructure, mechanical properties, strengthening, and deformation mechanisms of the as-deposited iHEA-Nb sample were systematically investigated using multiscale characterization approaches including EBSD, SEM, SXRD, (S)TEM, and mechanical testing. The main conclusions are as follows:

(1) The LMD-built iHEA-Nb sample exhibited a predominant fcc phase with [110] crystallographic texture along the deposition direction, and the *in situ* formation of NbC, $M_{23}C_6$, and M_7C_3 carbides was also detected. The typical characteristics of heterogeneous

microstructure were observed, including epitaxially grown elongated grains and fine equiaxed grains at the laser trajectory and layer interfaces, cellular microstructure, and element segregation at subgrain boundaries. The incorporation of Nb in the alloy matrix increased the degree of lattice distortion, the dislocation density as well as the number density of precipitates.

(2) The LMD-built iHEA-Nb sample showed an excellent synergy of high strength and high ductility at room temperature. The yield strength, ultimate tensile strength, and elongation reached 1140 MPa, 1450 MPa, and 31%, respectively, pushing the boundaries of the tensile properties and outperforming other HEAs produced by other additive manufacturing methods. Enhanced work hardening rate was also observed.

(3) The improved mechanical properties due to Nb addition are attributed to the introduction of the NbC reinforcing phase on one hand, and the simultaneous activation of multiple strengthening and deformation mechanisms on the other hand, including solid solution strengthening, precipitation strengthening, dislocation strengthening, and deformation twinning-induced plasticity effects.

(4) In the micropillar compression test, it was confirmed that the addition of Nb enhanced the critical resolved shear stress for both twining and slip, resulting in a lower density of mechanical twins after deformation compared with the Nb-free iHEA sample. The compressive strength of single crystals with different orientations was significantly improved after Nb addition.

Declaration of Competing Interest

The authors declare that they have no known competing financial interests or personal relationships that could have appeared to influence the work reported in this paper.

Acknowledgment

WZ acknowledges the China Scholarship Council for her PhD grant (CSC No. 201906250212). YP acknowledges financial support by Samenwerkingsverband Noord-Nederland (SNN) within the program “3D Print Kompas”. JPO and JS acknowledge Fundação para a Ciência e a Tecnologia (FCT-MCTES) for its financial support via the project UID/00667/2020 (UNIDEMI). JPO acknowledges funding by national funds from FCT - Fundação para a Ciência e a Tecnologia, I.P., in the scope of the projects Nos. LA/P/0037/2020, UIDP/50025/2020, and UIDB/50025/2020 of the Associate Laboratory Institute of Nanostructures, Nanomodelling and Nanofabrication – i3N. JS acknowledges the China Scholarship Council for her PhD grant (CSC No. 201808320394). The authors acknowledge DESY (Hamburg, Germany), a member of the Helmholtz Association HGF, for the provision of experimental facilities. Beamtime was allocated for proposal I-20210899 EC. The research leading to this result has been supported by the project CALIPSOplus under Grant Agreement 730872 from the EU Framework Programme for Research and Innovation HORIZON 2020. SF acknowledges financial support from the National Natural Science Foundation of China (No. 52105318) and Fundamental Research Funds for the Central Universities (Youth Teacher International Exchange & Growth Program No. QNXM20220027).

This research was carried out under project number S17024o in the framework of the Partnership Program of the Materials Innovation Institute M2i (www.m2i.nl) and the Netherlands Organization for Scientific Research (www.nwo.nl).

References

[1] B. Cantor, I.T.H. Chang, P. Knight, A.J.B. Vincent, Mater. Sci. Eng. A (2004) 213–218.

[2] J.W. Yeh, S.K. Chen, S.J. Lin, J.Y. Gan, T.S. Chin, T.T. Shun, C.H. Tsau, S.Y. Chang, Adv. Eng. Mater. 6 (2004) 299–303.

[3] Z. Li, D. Raabe, JOM 69 (2017) 2099–2106.

[4] L.J. Santodonato, P.K. Liaw, R.R. Unocic, H. Bei, J.R. Morris, Nat. Commun. 9 (2018) 4520.

[5] H. Hardraba, Z. Chlup, A. Dlouhy, F. Dobes, P. Roupcova, M. Vilemova, J. Matejicek, Mater. Sci. Eng. A 689 (2017) 252–256.

[6] T. Nagase, M. Todai, T. Hori, T. Nakano, J. Alloys Compd. 753 (2018) 412–421.

[7] Y.K. Kim, J.H. Yu, H.S. Kim, K.A. Lee, Comp. Part B 210 (2021) 108638.

[8] Y.F. Juan, J. Li, Y.Q. Jiang, W.L. Jia, Z.J. Lu, Appl. Surf. Sci. 465 (2019) 700–714.

[9] L.L. Hou, J.T. Hui, Y.H. Yao, J. Chen, J.N. Liu, Vacuum 164 (2019) 212–218.

[10] K. Zhou, Z. Wang, F. He, S. Liu, J. Li, J.J. Kai, J. Wang, Addit. Manuf. 35 (2020) 101410.

[11] S.W. Wu, G. Wang, Q. Wang, Y.D. Jia, J. Yi, Q.J. Zhai, J.B. Liu, B.A. Sun, H.J. Chu, J. Shen, P.K. Liaw, C.T. Liu, T.Y. Zhang, Acta Mater. 165 (2019) 444–458.

[12] Z. Li, C.C. Tasan, H. Springer, B. Gault, D. Raabe, Sci. Rep. 7 (2017) 40704.

[13] W. Zhang, H. Wang, B.J. Kooi, Y. Pei, Mater. Sci. Eng. A 872 (2023) 144978.

[14] F. Haftlang, H.S. Kim, Mater. Des. 211 (2021) 110161.

[15] V. Ocelík, N. Janssen, S.N. Smith, J.T.M. De Hosson, JOM 68 (2016) 1810–1818,

[16] J. Joseph, N. Stanford, P. Hodgson, D.M. Fabijanic, J. Alloys Compd. 726 (2017) 885–895.

[17] W. Zhang, A. Chabok, B.J. Kooi, Y. Pei, Mater. Des. 220 (2022) 110875.

[18] K. Zhou, J. Li, L. Wang, H. Yang, Z. Wang, J. Wang, Intermetallics 114 (2019) 106592.

[19] T. Yang, Y.L. Zhao, Y. Tong, Z.B. Jiao, J. Wei, J.X. Cai, X.D. Han, D. Chen, A. Hu, J.J. Kai, K. Lu, Y. Liu, C.T. Liu, Science 362 (2018) 933–937.

[20] F. He, B. Han, D. Chen, Q. Wu, Z. Wang, S. Wei, D. Wei, J. Wang, C.T. Liu, J.-j. Kai, Acta Mater. 167 (2019) 275–286.

[21] J.Y. He, H. Wang, H.L. Huang, X.D. Xu, M.W. Chen, Y. Wu, X.J. Liu, T.G. Nieh, K. An, Z.P. Lu, Acta Mater. 102 (2016) 187–196.

[22] S.G. Ma, Y. Zhang, Mater. Sci. Eng. A 532 (2012) 480–486.

[23] H. Jiang, L. Li, Z. Ni, D. Qiao, Q. Zhang, H. Sui, Mater. Chem. Phys. 290 (2022) 126631.

[24] N. Malatji, A.P.I. Popoola, T. Lengopeng, S. Pityana, Int. J. Miner. Metall. Mater. 27 (2020) 1332–1340.

[25] C.M. Zhao, H. Wu, J.F. Zhang, H.G. Zhu, Z.H. Xie, Rare Met. Mater. Eng. 50 (2021) 2783–2788.

[26] H. Jiang, D. Qiao, Y. Lu, Z. Ren, Z. Cao, T. Wang, T. Li, Scr. Mater. 165 (2019) 145–149.

[27] A. Chabok, W. Zhang, J. Shen, J.P. Oliveira, H. Wang, S. Feng, N. Schell, B.J. Kooi, Y.T. Pei, Addit. Manuf. 79 (2024) 103914.

[28] M.S.K.K.Y. Nartu, A. Jagetia, V. Chaudhary, S.A. Mantri, E. Ivanov, N.B. Dahotre, R.V. Ramanujan, R. Banerjee, Scr. Mater. 187 (2020) 30–36.

[29] F. Haftlang, E.S. Kim, J. Kwon, Y.U. Heo, H.S. Kim, Addit. Manuf. 63 (2023) 103421.

[30] T. DebRoy, H.L. Wei, J.S. Zuback, T. Mukherjee, J.W. Elmer, J.O. Milewski, A.M. Beese, A. Wilson-Heid, A. De, W. Zhang, Prog. Mater. Sci. 92 (2018) 112–224.

[31] Z. Yan, K. Zou, M. Cheng, Z. Zhou, L. Song, J. Mater. Res. Technol. 15 (2021) 582–594.

[32] S.C. Luo, P. Gao, H.C. Yu, J.J. Yang, Z.M. Wang, X.Y. Zeng, J. Alloys Compd. 771 (2019) 387–397.

[33] Q.Y. Lin, X.H. An, H.W. Liu, Q.H. Tang, P.Q. Dai, X.Z. Liao, J. Alloys Compd. 709 (2017) 802–807.

[34] Z. Li, C. Jing, Y. Feng, Z. Wu, T. Lin, J. Zhao, Int. J. Refract. Met. Hard Mater. 110 (2023) 105992.

[35] G. Reinhart, N. Mangelinck-Noël, H. Nguyen-Thi, T. Schenk, J. Gastaldi, B. Billia, P. Pino, J. Härtwig, J. Baruchel, Mater. Sci. Eng. A 413–414 (2005) 384–388.

[36] J.M. Park, J. Choe, J.G. Kim, J.W. Bae, J. Moon, S. Yang, K.T. Kim, J.H. Yu, H.S. Kim, Mater. Res. Lett. 8 (2019) 1638844.

[37] O. Andreau, I. Koutiri, P. Peyre, J.-D. Penot, N. Saintier, E. Pessard, T.D. Terris, C. Dupuy, T. Baudin, J. Mater. Process. Technol. 264 (2019) 21–31.

[38] J.J. Marattukalam, D. Karlsson, V. Pacheco, P. Beran, U. Wiklund, U. Jansson, B. Hjörvarsson, M. Sahlberg, Mater. Des. 193 (2020) 108852.

[39] J.M. Park, J. Choe, H.K. Park, S. Son, J. Jung, T.S. Kim, J.H. Yu, J.G. Kim, H.S. Kim, Addit. Manuf. 35 (2020) 101333.

[40] S. Bahl, S. Mishra, K.U. Yaza, I.R. Kola, K. Chatterjee, S. Suwas, Addit. Manuf. 28 (2019) 65–77.

[41] Z. Wu, C.M. Parish, H. Bei, J. Alloys Compd. 647 (2015) 815–822.

[42] Z. Sun, X. Tan, S.B. Tor, C.K. Chua, NPG Asia Mater. 10 (2018) 127–136.

[43] H. Wang, Z.G. Zhu, H. Chen, A.G. Wang, J.Q. Liu, H.W. Liu, R.K. Zheng, S.M.L. Nai, S. Primig, S.S. Babu, S.P. Ringer, X.Z. Liao, Acta Mater. 196 (2020) 609–625.

[44] Y.K. Kim, M.C. Kim, K.A. Lee, J. Mater. Sci. Technol. 97 (2022) 10–19.

[45] D. Kong, C. Dong, S. Wei, X. Ni, L. Zhang, R. Li, L. Wang, C. Man, X. Li, Addit. Manuf. 38 (2021) 101804.

[46] P. Ji, Z. Wang, Y. Mu, Y. Jia, G. Wang, Mater. Des. 224 (2022) 111326.

[47] J.X. Fang, J.X. Wang, Y.J. Wang, H.T. He, D.B. Zhang, Y. Cao, Mater. Sci. Eng. A 847 (2022) 143319.

[48] U. Pietsch, O.H. Seeck, Opt. Precis. Eng. 15 (2007) 1900–1907.

[49] I. Toda-Caraballo, P.E.J. Rivera-Díaz-del-Castillo, Acta Mater. 85 (2015) 14–23.

[50] F. Yang, L. Dong, X. Hu, X. Zhou, F. Fang, Z. Xie, J. Jiang, Mater. Lett. 275 (2020) 128154.

[51] Z. Tong, X. Ren, J. Jiao, W. Zhou, Y. Ren, Y. Ye, E.A. Larson, J. Gu, J. Alloys Compd. 785 (2019) 1144–1159.

[52] T.A. Rodrigues, J.D. Escobar, J. Shen, V.R. Duarte, G.G. Ribamar, J.A. Avila, E. Maawad, N. Schell, T.G. Santos, J.P. Oliveira, Addit. Manuf. 48 (2021) 102428.

[53] E. Abbasi, K. Dehghani, J. Alloys Compd. 783 (2019) 292–299.

[54] N. Gao, D.H. Lu, Y.Y. Zhao, X.W. Liu, G.H. Liu, Y. Wu, G. Liu, Z.T. Fan, Z.P. Lu, E.P. George, J. Alloys Compd. 792 (2019) 1028–1035.

[55] Y. Bai, D. Jiao, J. Li, Z. Yang, Mater. Today Commun. 31 (2022) 103554.

[56] W.M. Rainfortha, M.P. Blacka, R.L. Higginsona, E.J. Palmierea, C.M. Sellarsa, I. Prabstb, P. Warbichlerb, F. Hofer, Acta Mater. 50 (2002) 735–747.

[57] S. Gorsse, C. Hutchinson, M. Goune, R. Banerjee, Sci. Technol. Adv. Mater. 18 (2017) 584–610.

[58] J. Shen, J.G. Lopes, Z. Zeng, Y.T. Choi, E. Maawad, N. Schell, H.S. Kim, R.S. Mishra, J.P. Oliveira, Mater. Sci. Eng. A 872 (2023) 144946.

[59] X.Z. Zhang, T.J. Chen, Y.H. Qin, Mater. Des. 99 (2016) 182–192.

[60] R.U. Vaidya, K.K. Chawla, Compos. Sci. Technol. 50 (1994) 13–22.

[61] H. Wu, S. Huang, C. Zhao, H. Zhu, Z. Xie, C. Tu, X. Li, Intermetallics 127 (2020) 106983.

[62] J.F. Tu, C-J. Carbon Res. 4 (2018) 19.

[63] P. Poza, J. Gomez-Garcia, C.J. Munez, Acta Mater. 60 (2012) 7197–7206.

[64] X. Zhang, F. Meng, J.R. Christianson, C. Arroyo-Torres, M.A. Lukowski, D. Liang, J.R. Schmidt, S. Jin, Nano Lett. 14 (2014) 3047–3054.

[65] K. Wieczerzak, P. Bala, R. Dziurka, T. Tokarski, G. Cios, T. Koziel, L. Gondek, J. Alloys Compd. 698 (2017) 673–684.

[66] G. Chen, R. Rahimi, M. Harwarth, M. Motylenko, G. Xu, H. Biermann, J. Mola, Scr. Mater. 213 (2022) 114597.

[67] R. Rahimi, O. Volkova, H. Biermann, J. Mola, Adv. Eng. Mater. 21 (2019) 1800658.

[68] R. Rahimi, B.C. De Cooman, H. Biermann, J. Mola, Mater. Sci. Eng. A 618 (2014) 46–55.

[69] M.H. Lewis, B. Hattersley, Acta Metall. 13 (1965) 1159–1168.

[70] L. Zheng, X. Hu, X. Kang, D. Li, Mater. Des. 78 (2015) 42–50.

[71] H. Li, Philos. Mag. 96 (2016) 551–559.

[72] M. Wang, Y. Chiu, I. Jones, N. Rowlands, J. Holland, Z. Zhang, D. Flahaut, J. Phys. Conf. Ser. 522 (2014) 012034.

[73] W.X. Zhao, D.Q. Zhou, S.H. Jiang, H. Wang, Y. Wu, X.J. Liu, X.Z. Wang, Z.P. Lu, Mater. Sci. Eng. A 738 (2018) 295–307.

[74] P. Mannan, G. Casillas, E.V. Pereloma, Mater. Sci. Eng. A 700 (2017) 116–131.

[75] K. Lu, L. Lu, S. Suresh, Science 324 (2009) 349–352.

[76] C.Y. Chen, H.W. Yen, F.H. Kao, W.C. Li, C.Y. Huang, J.R. Yang, S.H. Wang, Mater. Sci. Eng. A 499 (2009) 162–166.

[77] E. Povolyaeva, S. Mironov, D. Shaysultanov, N. Stepanov, S. Zherebtsov, Mater. Sci. Eng. A 836 (2022) 142720.

[78] F. Haftlang, P. Asghari-Rad, J. Moon, A. Zargaran, K.A. Lee, S.J. Hong, H.S. Kim, Scr. Mater. 202 (2021) 114013.

[79] D. Raabe, C.C. Tasan, E.A. Olivetti, Nature 575 (2019) 64–74.

[80] Y.H. Jo, W.M. Choi, D.G. Kim, A. Zargaran, S.S. Sohn, H.S. Kim, B.J. Lee, N.J. Kim, S. Lee, Sci. Rep. 9 (2019) 2948.

[81] J.M. Park, E.S. Kim, H. Kwon, P. Sathiyamoorthi, K.T. Kim, J.-H. Yu, H.S. Kim, Addit. Manuf. 47 (2021) 102283.

[82] X. Gao, Z. Yu, W. Hu, Y. Lu, Z. Zhu, Y. Ji, Y. Lu, Z. Qin, X. Lu, J. Alloys Compd. 847 (2020) 156563.

[83] M.A. Melia, J.D. Carroll, S.R. Whetten, S.N. Esmaeely, J. Locke, E. White, I. Anderson, M. Chandross, J.R. Michael, N. Argibay, E.J. Schindelholz, A.B. Kustas, Addit. Manuf. 29 (2019) 100833.

[84] X. Zhang, R. Li, L. Huang, A. Amar, C. Wu, G. Le, X. Liu, D. Guan, G. Yang, J. Li, Vacuum 187 (2021) 110111.

[85] Y. Bai, H. Jiang, K. Yan, M. Li, Y. Wei, K. Zhang, B. Wei, J. Mater. Sci. Technol. 92 (2021) 129–137.

[86] J. Li, S. Xiang, H. Luan, A. Amar, X. Liu, S. Lu, Y. Zeng, G. Le, X. Wang, F. Qu, C. Jiang, G. Yang, J. Mater. Sci. Technol. 35 (2019) 2430–2434.

[87] F. Yang, L. Wang, Z. Wang, Q. Wu, K. Zhou, X. Lin, W. Huang, J. Mater. Sci. Technol. 106 (2022) 128–132.

[88] S. Luo, C. Zhao, Y. Su, Q. Liu, Z. Wang, Addit. Manuf. 31 (2020) 100925.

[89] Z.G. Zhu, X.H. An, W.J. Lu, Z.M. Li, F.L. Ng, X.Z. Liao, U. Ramamurty, S.M.L. Nai, J. Wei,

Mater. Res. Lett. 7 (2019) 453–459.

[90] T. Ikeda, M. Yonehara, T.-T. Ikeshoji, T. Nobuki, M. Hatate, K. Kuwabara, Y. Otsubo, H. Kyogoku, Crystals 11 (2021) 549.

[91] X. Yang, Y. Zhou, S. Xi, Z. Chen, P. Wei, C. He, T. Li, Y. Gao, H. Wu, Mater. Sci. Eng. A 767 (2019) 138382.

[92] D. Lin, L. Xu, X. Li, H. Jing, G. Qin, H. Pang, F. Minami, Addit. Manuf. 35 (2020) 101340.

[93] K. Kuwabara, H. Shiratori, T. Fujieda, K. Yamanaka, Y. Koizumi, A. Chiba, Addit. Manuf. 23 (2018) 264–271.

[94] P. Wang, P. Huang, F.L. Ng, W.J. Sin, S. Lu, M.L.S. Nai, Z. Dong, J. Wei, Mater. Des. 168 (2019) 107576.

[95] Y.L. Wang, L. Zhao, D. Wan, S. Guan, K.C. Chan, Mater. Sci. Eng. A 825 (2021) 141871.

[96] T. Fujieda, H. Shiratori, K. Kuwabara, M. Hirota, T. Kato, K. Yamanaka, Y. Koizumi, A. Chiba, S. Watanabe, Mater. Lett. 189 (2017) 148–151.

[97] Q. Shen, X. Kong, X. Chen, Mater. Sci. Eng. A 815 (2021) 141257.

[98] S. Kang, J.-G. Jung, Y.-K. Lee, Mater. Trans. 53 (2012) 2187–2190.

[99] E.P. Kwon, D.Y. Kim, H.K. Park, J. Mater. Eng. Perform. 26 (2017) 4500–4507.

[100] H.-W. Yen, M. Huang, C.P. Scott, J.-R. Yang, Scr. Mater. 66 (2012) 1018–1023.

[101] S. Lu, Q. Hu, B. Johansson, L. Vitos, Acta Mater. 59 (2011) 5728–5734.

[102] K. Ishida, Phys. Status Solidi. A 36 (1976) 717–728.

[103] L. Vitos, J.O. Nilsson, B. Johansson, Acta Mater. 54 (2006) 3821–3826.

[104] M. Mohammadzadeh, R. Mohammadzadeh, Appl. Phys. A 123 (2017) 720.

[105] D. Li, S. Song, Q. Liu, Q. Bai, G. Wu, N. Lv, Y. Lv, Y. Feng, F. Ren, Trans. Mater. Heat. Treat. 36 (2015) 105–111.

[106] I.G. Urrutia, D. Raabe, Scr. Mater. 66 (2012) 992–996.

[107] R. Mohammadzadeh, M. Mohammadzadeh, Mater. Sci. Eng. A 747 (2019) 265–275.

[108] R. Ueji, N. Tsuchida, D. Terada, N. Tsuji, Y. Tanaka, A. Takemura, K. Kunishige, Scr. Mater. 59 (2008) 963–966.

[109] J. Chen, F. Dong, Z. Liu, G. Wang, J. Mater. Res. Technol. 10 (2021) 175–187.

[110] G. Laplanche, A. Kostka, O.M. Horst, G. Eggeler, E.P. George, Acta Mater. 118 (2016) 152–163.

[111] X. Fu, X. Wu, Q. Yu, Mater. Today Nano 3 (2018) 48–53.

Declaration of competing interest

The authors declare that they have no known competing financial interests or personal relationships that could have appeared to influence the work reported in this paper.